Tension-induced suppression of allosteric conformational changes explains coordinated stepping of kinesin-1

Tsukasa Makino[1,2,3], Ryo Kanada[4], Teppei Mori[1], Ken-ichi Miyazono[2], Yuta Komori[3], Haruaki Yanagisawa[3], Shoji Takada[4], Masaru Tanokura[2], Masahide Kikkawa[3], and Michio Tomishige[1,5]

[1]*Department of Applied Physics, The University of Tokyo, Tokyo, Japan*
[2]*Department of Applied Biological Chemistry, Graduate School of Agricultural and Life Sciences, The University of Tokyo, Tokyo, Japan*
[3]*Department of Cell Biology and Anatomy, Graduate School of Medicine, The University of Tokyo, Tokyo, Japan*
[4]*Department of Biophysics, Graduate School of Science, Kyoto University, Kyoto, Japan*
[5]*Department of Physical Sciences, College of Science and Engineering, Aoyama Gakuin University, Sagamihara, Japan*

Correspondence to Michio Tomishige: tomishige@phys.aoyama.ac.jp
R. Kanada's current affiliation is RIKEN Center for Computational Science, Kobe, Japan

Abstract

The dimeric motor protein kinesin-1 walks along microtubules by alternating ATP hydrolysis and movement of its two motor domains (“head”). The detached head preferentially binds to the forward tubulin-binding site after ATP binds to the microtubule-bound head, but the mechanism preventing premature binding to the microtubule while the partner head awaits ATP remains unknown. Here, we examined the role of the neck linker, the segment connecting the two heads, in this mechanism. High-resolution structural analyses of the nucleotide-free head revealed a bulge just ahead of the neck linker’s base that creates an asymmetric constraint on its mobility. While the neck linker can stretch freely backward, it must navigate around this bulge to extend forward. Based on this finding, we hypothesized that premature binding of the tethered head is suppressed by an intolerable increase in neck linker tension. Molecular dynamic simulations and single-molecule fluorescent assays supported this model. These findings demonstrate a tension-based regulation mechanism where off-pathway conformational transitions are thermodynamically suppressed through entropy loss associated with neck linker stretching, suggesting that neck linker tension influences the allosteric conformational transition rather than directly affecting the nucleotide state.

Introduction

Kinesin-1 (hereafter referred to as kinesin) is a dimeric motor protein that transports cargo inside cells by moving toward the plus-end of the microtubule (Vale, 2003). Kinesin is a highly processive motor, capable of taking over 100 consecutive 8-nm steps before detaching from the microtubule. The unidirectional and processive motion of kinesin is powered by a hand-over-hand movement of two motor domains ("heads") (Kaseda et al., 2003, Asbury et al., 2003; Yildiz et al., 2004). After the trailing head detaches from the microtubule, it surpasses the partner head and attaches to the forward-tubulin binding site located 16 nm ahead. The binding and dissociation of the head to and from the microtubule are tightly coupled to its ATP turnover; ADP release stabilizes the microtubule binding of the head, while ATP hydrolysis and phosphate release cause the head to detach from the microtubule (Cross, 2004; Cochran 2015). Consequently, for the kinesin to move hand-over-hand, the ATP hydrolysis cycles of the two heads must be out of phase.

In his elegant experiment, Hackney demonstrated that when a kinesin dimer encounters a microtubule, it releases ADP from only one of its heads (Hackney, 1994). Subsequent ATP binding to the microtubule-bound head is required to release ADP from the second head. This suggests that before ATP binding, one head is bound to the microtubule and is nucleotide-free, and the other head, still bound to ADP, is tethered by its partner. ATP binding to the microtubule-bound head then aids the tethered head in attaching to the microtubule.

To illustrate the ATP-induced stepping of the tethered head, a model involving a conformational change in the neck linker region, a 14 amino-acid stretch that connects the two heads, has been proposed (Vale and Milligan, 2000). The neck linker has been shown to undergo a disordered-to-ordered structural transition depending on the nucleotide state of the head (Rice et al., 1999). In the ATP or ADP·Pi state, the neck linker is docked onto the head, with its distal end pointing forward, whereas in the nucleotide-free or ADP state, it detaches from the head, becoming disordered. This discovery led to the model that docking of the neck linker to the microtubule-bound

head upon ATP-binding moves the tethered head forward, and the subsequent diffusional search of the tethered head allows it to bind to the forward-tubulin binding site. This mechanism explains how the tethered head preferentially binds to the forward-binding site after ATP binding to the microtubule-bound, leading head. However, it does not clarify how the tethered head is prevented from rebinding to the rear-tubulin binding site before ATP binds to the leading head.

The original neck linker docking model, therefore, hypothesized that the ADP-bound trailing head, after Pi release, is not away from the tubulin-binding site; instead, it's still weakly bound to the microtubule, maintaining a two-head-bound state (Hancock and Howard, 1999; Vale and Milligan, 2000; Shief et al., 2004). The neck linker docking of the leading head facilitates the dissociation of the trailing head from the microtubule, translating the head forward. However, three laboratories using different single-molecule techniques led to the conclusion that under limited ATP concentrations, the kinesin dimer stably assumes a one-head-bound state, in which the trailing head is displaced from the rear-tubulin binding site while waiting for ATP binding (Mori et al., 2007; Guydosh and Block, 2009; Asenjo et al., 2009). More recent studies with high temporal resolution single-molecule observations of one of the kinesin heads further demonstrated that kinesin waits for ATP-binding in the one-head-bound state under a wide range of ATP concentrations, including saturating ATP conditions (Isojima et al., 2016; Wolff et al., 2023).

These experiments provided in-depth information about the structural state of the ATP waiting state; the tethered head is positioned on average to the right and slightly behind the microtubule-bound head (Mori et al., 2007; Isojima et al., 2016; Wolff et al., 2023), and has a significant translational and rotational freedom (Guydosh and Block 2009; Asenjo et al., 2009; Isojima et al, 2016). These findings about the ATP-waiting state provoke a question: How is the tethered head's rebinding to the rear-tubulin binding site prevented before ATP-binding to the microtubule-bound head? When the neck linkers were artificially extended by inserting spacers between the neck linker and the coiled-coil stalk, the kinesin dimer could release both ADPs rapidly, even without added ATP (Hackney et al., 2003; Andreasson et al., 2015), and the tethered head could bind to rear

102 and forward-tubulin binding sites before ATP-binding to the microtubule-bound head
103 (Yildiz et al., 2008; Isojima et al., 2016). In the two-head-bound state of wild-type
104 kinesin, the neck linkers of the front and rear heads are stretched in opposite directions
105 due to their limited length (Benoit et al., 2021). These findings suggest that constraints
106 on the neck linker (whether from steric hindrance or interactions with the head or
107 microtubule) are crucial in preventing the tethered head from binding to microtubule.
108
109 To understand the mechanism that prevents premature binding of the tethered head to
110 the microtubule during ATP-waiting state, we first studied the neck linker conformation
111 in the nucleotide-free state using X-ray crystallography and cryo-electron microscopy
112 (cryo-EM). We found that the motility of the neck linker in the nucleotide-free state is
113 asymmetrically constrained due to a steric hindrance from the motor domain, which
114 impacts the neck linker's extensibility toward the plus-end of the microtubule. Using
115 this structural information, we built a model of dimeric kinesin in a two-head-bound
116 state where both heads are nucleotide-free. Comparing this with the two-head-bound
117 state with an ATP-bound trailing head and a nucleotide-free leading head, we theorized
118 that excessive increase in neck linker tension prevents the transition to the two-head-
119 bound state where both heads are nucleotide-free. We tested this hypothesis using
120 molecular dynamic (MD) simulation and single-molecule fluorescence resonance
121 energy transfer (smFRET). These results suggest a tension-based mechanism that
122 controls the transition from one-head-bound to two-head-bound states, as well as
123 transitions between two-head-bound states; among possible conformational transitions,
124 the one that requires less entropy reduction from stretching the disordered neck linker is
125 favored.
126

127 ## Results

128 **Structural analysis of the neck linker in nucleotide-free state**

129 The crystal structure of the nucleotide-free kinesin-1 motor domain has been solved as a
130 complex with tubulin (Cao et al., 2014) and as mutant kinesins (Cao et al., 2017).
131 However, the neck linker was truncated in these constructs, leaving the high-resolution
132 structure of the kinesin-1 neck linker in the nucleotide-free state unclear. Here, we

133 analyzed the structure of a human kinesin-1 construct of 336 amino acids, which
134 includes the N-terminal motor domain (1-322 residues) and the subsequent neck linker
135 (323-336 residues), using X-ray crystallography. For consistency across experimental
136 techniques and comparison with the previously solved nucleotide-free kinesin-1
137 structures, we used a cysteine-light mutant kinesin, where surface-exposed cysteines
138 were replaced with either Ala or Ser (Rice et al., 1999; Tomishige and Vale, 2000).
139 Since kinesin in solution tightly binds ADP and becomes unstable in the absence of
140 both nucleotide and microtubule (Cross, 2004), we used a G234A mutant kinesin, in
141 which Gly234 residue in the switch II loop was replaced with Ala. This mutant is
142 known to rapidly release ADP, even in the absence of microtubules (Rice et al., 1999).
143
144 First, we verified that the G234A and cysteine-light mutations did not alter the structure
145 of the kinesin motor domain in an ADP-bound state (Fig. 1 A). We then successfully
146 crystallized the G234A mutant kinesin under a nucleotide-free condition. The X-ray
147 crystal structure was determined at a 2.8 Å resolution (Fig. 1 B; and Table 1). The
148 electron density map of the nucleotide-binding pocket revealed the absence of a
149 nucleotide or an ion that mimics inorganic phosphate (Fig. S1). The overall structure of
150 the G234A motor domain was similar to that of the previously solved nucleotide-free
151 kinesin-1 (Cao et al., 2014) (Fig. 1 B). The neck linker, directly following the α6-helix
152 of the motor domain, was only visible for the initial two residues (K323 and T324) (Fig.
153 1 C); the rest of the neck linker was disordered, consistent with the previous reports
154 (Rice et al., 1999; Tomishige et al., 2006). The observed neck linker structure was
155 independent of crystal packing effects, as the nearest element of the adjacent chain (L5)
156 was 1.1 nm away from the K324 residue. The position of T324 is stabilized by a
157 hydrogen bond with the side chain of R321 residue of α6. In the ADP·AlF_4-bound state,
158 these residues fold into an extra turn of α6-helix (Fig. 1 D), while in the nucleotide-free
159 state, the α4 helix, which lies vertically to the α6 helix, sterically prevents the α-helix
160 formation of these residues. Consequently, the unfolded K323 and T324 residues are
161 excluded from the motor domain and point away from the core (Fig. 1 C). Similar
162 results were obtained using a crystal structure of G234V mutant (Fig. S2).
163

164 Next, we analyzed the structure of kinesin in complex with microtubule using cryo-EM
165 to elucidate how the microtubule influences the neck linker configuration. Cysteine-
166 light kinesin-1 construct of 349 amino acids was bound to microtubule under
167 nucleotide-free conditions, and its structure was reconstituted at a 3.48 Å resolution
168 (Fig. 2 A-C; Fig. S3), better than that of the previously reported cryo-EM structure of
169 nucleotide-free kinesin-1 (Shang et al., 2014). The atomic model was built using a
170 flexible fitting with the crystal structures of the nucleotide-free G234A and GMPPNP-
171 bound microtubule. The refined model closely resembles the previously reported crystal
172 structure of nucleotide-free kinesin-tubulin complex (Cao et al., 2014), except that the
173 N-terminus of α4, which extends upon microtubule-binding, along with L11, is nearly
174 straight in our structure but distorted toward the plus-end in the Cao et al.'s structure
175 (Fig. 2, D and E). The discrepancy can be explained by the fact that Cao et al.'s kinesin
176 is bound to curved tubulin, whereas our cryo-EM model is on the straight microtubule
177 and better describes the interactions in the kinesin-tubulin interface (Fig. 2 F-H). The
178 neck linker is mostly disordered, with only the first two residues, K323 and T324,
179 visible (Fig. 2, B and C), consistent with results from the G234A mutant's crystal
180 structure. These findings suggest that the neck linker doesn't interact specifically or
181 stably with either the motor domain or the microtubule surface in the nucleotide-free
182 state.
183
184 **Structural feature of nucleotide-free motor domain peripheral to the neck linker**
185 We then turned our attention to the structural feature of the kinesin motor domain
186 unique in the nucleotide-free state, specifically those parts adjacent to the neck linker,
187 and studied how these parts influence the configuration of the disordered neck linker. In
188 previous research, Grant et al. classified 114 distinct chains from 69 kinesin family
189 crystal structures using principal component analysis and found that they are segregated
190 into two major groups (termed ATP-like and ADP-like conformational states) along
191 with a minor cluster that includes exclusively inhibitor-bound kinesin-5 (Grant et al.,
192 2007; Scarabelli et al., 2013). Here, we performed the principal component analysis on
193 247 polypeptide chains from 137 kinesin family crystal structures deposited in the
194 Protein Data Bank, which includes the nucleotide-free crystal structures by Cao et al.,
195 plus our nucleotide-free structures of kinesin-1 (G234A and G234V crystal and wild-

196 type cryo-EM structures). The 2D conformer plot of the first two principal components
197 shows that our nucleotide-free structures and those of Cao et al. form a distinct cluster
198 separate from the ATP-like and ADP-like states (Fig. 3, A and B), demonstrating that
199 these nucleotide-free structures represent a third conformational state of kinesin
200 structure. Other crystal structures of kinesin family proteins without bound nucleotide
201 (but with an ion bound to P-loop that may mimic phosphate) are classified into ADP-
202 like or ATP-like states (Shipley et al., 2004; Morikawa et al., 2015; Guan et al., 2017;
203 Cao et al., 2017).
204
205 The correlation between the bound-nucleotide and the conformational state of kinesin
206 crystal structures is not evident in the absence of microtubule (e.g., the ATP-like class
207 primarily consists of ADP-bound crystal structures). Moreover, a recent cryo-EM
208 analysis of KIF14 on the microtubule revealed that the AMP-PNP-bound motor domain
209 could adopt a conformation similar to the nucleotide-free head when its neck linker is
210 truncated or detached from the head (Benoit et al., 2021). Therefore, we adopted the
211 nomenclature of kinesin's three conformational states proposed by Sosa's group, which
212 is based on the openness of the nucleotide-binding pocket rather than the bound-
213 nucleotide (Benoit et al., 2023); we termed these three classes as open (which includes
214 our nucleotide-free structures), semi-open (formally known as ADP-like), and closed
215 (previously known as ATP-like) states (Fig. 3, C-E). We chose the term "semi-open"
216 over "semi-closed" to describe the ADP-like state because the angle of the subdomain,
217 which influences the openness of the nucleotide pocket, in the semi-open state is rather
218 similar to that of the open state (will be described later).
219
220 The conformational changes from open to closed states in kinesin-1 can be
221 approximated as relative rigid-body movements of three distinct subdomains, as
222 demonstrated by Cao et al. (Cao et al., 2014), although this previous analysis did not
223 include the semi-open state. Here, we identified the subdomains of kinesin-1 by
224 comparing representative structures from the open, closed, and semi-open states using a
225 domain-search program (Fig. 4 A). The three subdomains we identified differ from
226 those identified by Cao et al.; one of the domains remains nearly stationary on the
227 microtubule during the conformational changes between three states (we refer to this as

228 Bottom-domain or B-domain), and the other two domains move relative to the
229 stationary B-domain during the conformational changes (Fig. 4 B), which are spatially
230 divided into front and rear halves of the motor domain, with the central α4 helix as a
231 border (Fig. 4, C and D); therefore, we termed Front- and Rear-domains, or F- and R-
232 domains.
233
234 **Nucleotide-dependent subdomain motions affect the neck linker mobility**
235 The transition from semi-open to open conformation, coupled with the release of ADP
236 from the motor domain after microtubule-binding, results in anticlockwise rotational
237 movements of the F-domain when viewed from the minus-end, while the R-domain
238 rotates clockwise (Sindelar, 2011; Cao et al., 2014; Benoit et al., 2023; Fig. 4B; Video
239 1). The rotational movement of the R-domain (containing P-loop and α6 helix; Fig. 4 A)
240 relative to the B-domain (including α4 helix) leads to the opening of the nucleotide-
241 binding pocket located on the left side, and a steric clash between the C-terminus of α4
242 on the right side and the distal end of α6 where the neck linker is linked (Fig. 4, B and
243 C). This steric hindrance likely imposes an asymmetric constraint on the mobility of the
244 disordered neck linker (Fig. 4 D; Video 2). Specifically, the neck linker can stretch
245 freely backward (toward the microtubule's minus-end), while its forward mobility is
246 restricted by the steric hindrance from the C-terminus of α4 helix and subsequent L12.
247
248 To explore the hypothesis that the neck linker's mobility is asymmetrically constrained
249 in the nucleotide-free/open state, we visualized the position of the mobile neck linker in
250 the nucleotide-free state by labeling it with a gold cluster (Rice et al., 1999; Kikkawa et
251 al., 2000). To comprehend the influence of steric hindrance near the neck linker's
252 proximal end, a maleimide-modified gold cluster with a diameter of 1.4 nm was
253 attached to the thiol residue of T328C in a cysteine-light kinesin head, which is four
254 amino acids away from the last ordered neck linker's residue T324. A cryo-EM density
255 map with a resolution of 15 Å showed that the density corresponding to the gold cluster
256 appeared as an ellipsoidal shape extending along the microtubule protofilament (Fig. 5
257 A). The centroid of the gold density is 2.37 nm away from the T324 residue, a distance
258 consistent with the combined length of a 4 amino-acids peptide (approximately 1.5 nm),
259 the maleimide linker, and the gold cluster's radius. The gold density is located rearward

from the proximal end of the neck linker or the distal end of α6 helix and away from the microtubule surface. These observations support the hypothesis that, in the absence of a bound nucleotide, the mobility of the disordered neck linker is biased toward the minus end of the microtubule. This finding is also consistent with the right and rearward positioning of the tethered head relative to the microtubule-bound head in kinesin dimer during the ATP-waiting (Fig. 5 B; Mori et al., 2007; Isojima et al., 2016; Wolff et al., 2023).

Structural basis to prevent rebinding of the tethered head while waiting for ATP

The asymmetric constraint on the neck linker in the nucleotide-free/open state provides insights into the mechanism that prevents the transition to the two-head-bound state where both heads are nucleotide-free and in open conformation (termed T_{open}-L_{open} state) while waiting for ATP binding. Given that the contour length of one of the unfolded neck linkers is about 5.3 nm (assuming a contour length of 3.8A per amino acid (Hyeon and Onuchic, 2007; Hariharan and Hancock, 2009)), when both heads of kinesin dimer bind to adjacent tubulin-binding sites separated by 8.2 nm, the neck linker in the leading head stretches backward, while the one in the trailing head stretches forward (Benoit et al., 2021). We created a model of the kinesin dimer on a microtubule in the T_{open}-L_{open} state, where both heads are nucleotide-free and adopt the open conformation. First, the atomic models of two nucleotide-free heads were placed on the adjacent tubulin-binding sites and were connected by disordered neck linker chains (Fig. S4, A and B). Then, a typical configuration of the disordered neck linker chains in the thermal equilibrium state was estimated using MD simulations (Fig. S4 C; Video 3).

The neck linker of the leading nucleotide-free/open head stretches backward without steric hindrance; however, that of the trailing open head cannot go straight toward the plus-end of microtubule due to the steric hindrance posed by the α4 helix (Fig. 6 A, left). In the equilibrium configuration, the neck linker in the trailing head detours around to extend forward. Throughout the simulation, the stretched neck linker remained displaced from the head without any interaction, suggesting that the neck linker behaves as an entropic spring. To illustrate the difference between the neck linkers of trailing head in the open and closed conformational states, we also modeled

292 the kinesin dimer in the two-head-bound state where the trailing head is ATP-bound and
293 in the closed conformation (T_{close}-L_{open}; Fig. 6 A, right; Video 4). During this
294 simulation, we observed a stable contact between the K326 side chain of the disordered
295 neck linker and the D37 and F48 residues of the leading head (see Video 4), suggesting
296 that the neck linker tension in T_{close}-L_{open} state includes an energetic component. The
297 distance between T328 residue in the trailing head and I325 residue in the leading head
298 increases by 0.96 nm in T_{open}-L_{open} compared to T_{closed}-L_{open} (Fig. 6 A). Given that the
299 disordered polypeptide chain acts like an entropic spring, extending the end-to-end
300 distance of the disordered neck linker increases the tension applied to both ends. To
301 estimate the amount of this tension, we isolated the disordered neck linker segments
302 from both leading and trailing heads that stretch between the motor domains without
303 steric hindrance or docking onto the head (Fig. S4 D). Then, we applied a harmonic
304 potential to the Cα atoms at both ends of the stretched region and calculated the tension
305 from the average displacement of the Cα atom from the potential minimum using MD
306 simulations (Fig. 7, A and B). The calculated tension on the neck linker in T_{open}-L_{open}
307 was 98 pN, which is twice as much as in the T_{closed}-L_{open} state (39 pN; Fig. 7C). The
308 tension in the T_{closed}-L_{open} state is likely an overestimate since this measurement
309 excludes the enthalpic component discussed above, though it is comparable to previous
310 MD measurements and theoretical calculations using a worm-like chain model
311 (Hariharan and Hancock, 2009). Therefore, we hypothesized that the transition from the
312 one-head-bound state to the T_{open}-L_{open} two-head-bound state is thermodynamically
313 unfavorable because it would result in an intolerable increase in the tension applied to
314 the neck linker, while the transition to the T_{closed}-L_{open} state is feasible, as the tension
315 applied to the neck linker is lower and might be tolerable.
316
317 **Effect of tension of the neck linker on the tethered head binding**
318 The role of tension applied to the neck linker on processive motility of kinesin dimer
319 has been explored through the use of mutant kinesins with artificially extended neck
320 linkers. Past research found that the velocity of the mutant's processive motion
321 decreased, but the ATP turnover rate remained unchanged compared to the wild-type
322 (Yildiz et al., 2008; Shastry and Hancock, 2010; Clancy et al., 2011; Andreasson et al.,
323 2015). These findings are consistent with the above hypothesis, as it predicts that

324 reduced tension on the neck linker would facilitate the transition to the T_{open}-L_{open} state,
325 and additional ATP consumption is needed to return to the one-head-bound state,
326 impairing the coupling between ATP hydrolysis and the forward step. To gather more
327 direct evidence for this hypothesis, we systematically examined the relationship
328 between the amount of tension applied to the neck linker and the probability of
329 transitioning to two-head-bound states in the absence of ATP.
330
331 We used neck linker-extended mutants with varying levels of tension and observed their
332 impact on the transition to the T_{open}-L_{open} state. To increase the contour length of the
333 disordered neck linker, we inserted poly-Gly residues of different lengths between the
334 last two junctional residues of the neck linker (L335 and T336 residues; Fig. 8 A)
335 (Yildiz et al. 2008; Clancy et al., 2011; Isojima et al., 2016). Then, we used a single-
336 molecule FRET (smFRET) sensor to detect the transition between one-head-bound and
337 two-head-bound states of the neck-linker extended mutants. Cysteine residues were
338 introduced at the tip of one head (215Cys) and the base of another head (43Cys) on the
339 cysteine-light background and were labeled with donor and acceptor dyes (Fig. 8 A).
340 Previous studies showed that in the presence of a non-hydrolyzable ATP analogue,
341 kinesin with this smFRET sensor displayed low (10%) and high (90%) FRET
342 efficiencies, representing the two-head-bound state (Mori et al., 2007). In contrast, with
343 a low amount of ADP, kinesin exhibited a distinct median (~30%) FRET efficiency,
344 indicating a one-head-bound state. To occasionally revert the transition towards the one-
345 head-bound state and observe the ATP-independent transitions from one-head-bound to
346 two-head-bound state, the observations were carried out in the presence of 2 μM ADP
347 (ADP binds a few times per second, assuming ADP binding rate of 2 $\mu M^{-1}s^{-1}$ (Cross,
348 2004)).
349
350 SmFRET observations revealed that the kinesin mutant, which has its neck linkers
351 extended by inserting 3 poly-Gly residues (referred to as G3), frequently transitioned to
352 two-head-bound states and then reverted back to a one-head-bound state triggered by
353 occasional ADP-binding (Fig. 8 B). Under the same condition, the wild-type kinesin,
354 without neck linker extension (termed G0), rarely showed transitions to the two-head-
355 bound state. When the neck linker was further extended by 5 poly-Gly insertions, the

356 duration of the one-head-bound state became negligible (Fig. 8 B), resulting in the
357 mutant spending most of its time in two-head-bound states. The distribution of FRET
358 efficiency shows that the G5 mutant occupies both high and low FRET states (i.e., two-
359 head-bound states where either the donor- or acceptor-labeled head is leading) with
360 nearly equal probability (Fig. 8 C), indicating that the detached head can bind to both
361 forward and rearward tubulin-binding sites. The population of the medium FRET state
362 (one-head-bound state) decreased as the number of inserted residues increased, and the
363 two-head-bound states dominated for mutants with more than 5 poly-Gly insertions
364 (Fig. 8 C). We reasoned that the G5 mutant could transition quickly from one-head-
365 bound to T_{open}-L_{open} states due to a reduced tension applied to the neck linker compared
366 to the wild-type (98 pN). We used MD simulation to estimate this tension in the G5
367 mutant's T_{open}-L_{open} state and found that the tension was reduced to 19 pN (Fig. S5),
368 which is now comparable to that in the T_{closed}-L_{open} state of wild-type (39 pN). These
369 findings support the theory that the amount of tension applied to the neck linker is
370 critical in regulating the transition from one-head-bound to two-head-bound states.
371

372 **Discussion**

373 In the present study, we investigate the role of the neck linker in preventing the
374 premature binding of the unbound head to the microtubule before ATP-binding to the
375 leading head triggers the forward stepping of the head. High-resolution structural
376 observations and the principal component analysis of kinesin structures revealed that the
377 nucleotide-free structures belong to the distinct “open” conformational state (Fig. 3 A);
378 in this state, the bulge of the C-terminal end of α4 on the surface of the head is located
379 just forward from the C-terminus end of α6, to which the neck linker is attached (Fig. 4
380 D). This creates a steric hindrance when the neck linker is pulled forward but does not
381 interfere when it is pulled backward (Fig. 6 A). MD simulation demonstrated that the
382 tension applied to the neck linker in the T_{open}-L_{open} state is over twice as high as that in
383 the T_{close}-L_{open} state (Fig. 7 C). While the steric hindrance is small (approximately a 0.8
384 nm hemisphere), the tension increases significantly when the extension occurs during a
385 rapidly increasing phase of the nonlinear force-extension curve of the entropic spring
386 (Hariharan and Hancock, 2009). SmFRET observations of neck linker extended mutants

387 further support the notion that the transition from one-head-bound to two-head-bound
388 T_{open}-L_{open} state is prohibited due to an intolerable tension increase (Fig. 8).
389
390 This asymmetric constraint on the neck linker is relieved when ATP binds and the
391 kinesin motor domain transitions from open to closed state. During this transition, both
392 the Front- and Rear-domains rotate anticlockwise relative to the Bottom-domain (Cao et
393 al., 2014; Benoit et al., 2023; Fig. 4 B; Video 1). The R-domain, in particular,
394 showcases a substantial rotational movement that leads to the closure of the nucleotide
395 pocket on the left side and translates the distal end of α6 along with β1 away from α4 on
396 the right side (Sindelar, 2011). As a result, the distal end of the α6 helix has room to
397 extend, and K323 and T324 residues, previously excluded from the core in the
398 nucleotide-free state, now contribute to an additional half-turn of α6 (Figs. 1D and 4D;
399 Video 2). Simultaneously, the rotation of the F-domain unveils a hydrophobic pocket
400 between α4 and β1. The formation of the α-helix by K323 and T324 moves the
401 neighboring I325 residue close to the hydrophobic pocket and reorients its hydrophobic
402 side chain, allowing the Ile side chain to bind complementarily to the hydrophobic
403 pocket—an essential step in initiating neck linker docking (Vale and Milligan, 2000;
404 Cao et al., 2014, Benoit et al., 2023). Finally, the rotation of the F-domain exposes the
405 groove where the remainder of the neck linker forms two β-sheets and docks onto the
406 head, completing the neck linker docking.
407
408 Because the tension applied to the disordered neck linker is only effective during the
409 two-head-bound state, previous studies have mainly focused on how the tension of the
410 neck linker influences the transition from a two-head-bound to a one-head-bound state
411 (Block, 2007; Valentine and Gilbert, 2007; Gennerich and Vale, 2009). Here we show
412 that the tension applied to the neck linker is also essential in regulating the transition
413 from the one-head-bound to the two-head-bound state (Fig. 9, red rectangle). Since the
414 conformational state doesn't strictly correlate with the nucleotide state, in the following
415 section, we'll represent each state during the cycle as the nucleotide
416 state/conformational state. The tethered ADP-bound head is in the semi-open
417 conformational state and might transiently bind to the forward or rearward tubulin-
418 binding site relative to the microtubule-bound nucleotide-free/open head. We did not

estimate the tension in this two-head-bound state because the high-resolution structure of a semi-open state bound to the microtubule is not available as this state is unstable and transient (Benoit et al., 2021). Therefore, we can only speculate that the tension would lie somewhere between that of the T_{close}-L_{open} and T_{open}-L_{open} states, and that microtubule binding of the tethered semi-open head may be restricted because the disordered neck linkers would need to adopt highly stretched configurations. Even when the tethered head managed to bind to the microtubule, the conformational transition of the ADP-bound head from semi-open to open state is prohibited as it would associate a significant increase in the tension on the neck linker, thereby maintaining the one-head-bound state. ATP-binding to the microtubule-bound head then induces rotational movement of the R-domain, moving the C-terminal of α6 upward from the bulge of α4, diminishing the asymmetric constraint on the neck linker. Under this condition, the tethered head binds to the forward tubulin-binding site and can transit to an ADP-bound/open state because the neck linker tension in this state is tolerable, followed by rapid ADP release from the head. Here, we highlight that the neck linker tension influences the allosteric transitions among three conformational states, not the nucleotide state directly.

The transition from semi-open to open conformation associated with ADP release is thermodynamically favorable for a head without neck linker constraint upon encountering the microtubule (Cross, 2004; Atherton et al., 2014; Benoit et al., 2023). However, in the case of dimeric kinesin during processive movement, this transition is also influenced by the level of neck linker tension; if the entropy reduction caused by stretching the disordered neck linker region exceeds the free energy decrease associated with the semi-open to open conformational transition of the head upon microtubule binding, the transition would become thermodynamically unfavorable (i.e., the sum of the free energy change of the head and the disordered neck linker increases). When the neck linker tension is reduced by inserting more than 5 poly-Gly residues, the loss in entropy decreases, making the transition to the T_{open}-L_{open} state favorable.

This tension-based regulation mechanism (suppression of the thermodynamically favorable conformational transition by decreasing entropy) can be applied to other

allosteric conformational transitions that alter the extensibility of the neck linker. For instance, when ATP binds to the leading head of the T_{close}-L_{open} state (Fig. 9, purple rectangle), the transition of the leading head from open to closed conformation (T_{close}-L_{close} state) increases the neck linker tension from 39 pN to 125 pN, under the condition that only the initial segment (residues 323-325) of the neck linker is docked onto the head (Figs. 6 B and 7). We included the I325 residue as it is crucial to thermodynamically stabilize the hydrophobic pocket exposed to the solvent in the closed state (Vale and Milligan, 2000; Sindelar, 2011, Cao et al, 2014). This excessive increase in tension would even prevent the initial I325 residue from docking onto the head. Therefore, even after ATP binding, the closed state is unstable in the leading head, and the head remains in the ATP-bound/open state (Benoit et al., 2023), which may follow by reversible ATP release. This sharply contrasts with the trailing head in the T_{close}-L_{open} state, which is stabilized in the ATP-bound/closed state due to the forward strain applied to the neck linker, because the reverse transition of the trailing head from the ATP-bound/closed state to the ATP-bound/open state (from T_{close}--L_{open} to T_{open}-L_{open} state) is restricted by tension increase, as previously explained. ATP-hydrolysis and Pi release would then proceed in the stabilized closed nucleotide-pocket (Parke et al., 2010). Our kinetic measurements, which distinguished between leading and trailing heads, revealed that these heads are stabilized in low and high ATP-affinity state, respectively, and the neck linker strain controls the equilibrium between these states (Niitani et al., 2024). These findings further support the idea that neck linker tension influences the allosteric conformational transition, rather than directly affecting the nucleotide state. Hence, the tension-based regulation mechanism provides a rationale for the alternating catalysis of two heads during processive movement.

Moreover, this tension-based regulation mechanism provides a distinct mechanism from the neck linker docking model described earlier to explain the preferential forward stepping of the unbound head (Fig. 9, green hexagonal box). Assuming the microtubule-bound head binds ATP and transitioned to a closed state—while its neck linker remains detached—the tethered head can freely diffuse to both forward and rearward tubulin-binding sites. This assumption stems from the discovery of a relatively small free energy change associated with neck linker docking (Rice et al., 2003). However, the

transition from semi-open to open state happens only at the forward binding site. We created a model of the T_{open}-L_{close} dimer (after the tethered head binds to the rear binding site) where the leading head is in the closed state, but its neck linker is mostly detached from the head, leaving the first two amino acids to form an additional α6 helix (Fig. 6 C). The estimated tension in this state, according to an MD simulation, was 116 pN, which is even higher than that in the T_{open}-L_{open} state (Fig. 7). Thus, this transition is thermodynamically unfavorable, and the transition to the T_{close}-L_{open} state will likely occur instead. In this model, neck linker docking is not necessary to account for the differences in neck linker tension (or entropy reduction); instead, it relies on the presence or absence of steric hindrance near the base of the neck linker in the trailing head. This idea is consistent with the findings of Taniguchi et al. (2005), who observed temperature-dependent stepping under load and demonstrated that the directionality of the kinesin step primarily originated from an entropic asymmetry. The two mechanisms explaining preferential forward stepping are not mutually exclusive. However, the tension-based mechanism may be crucial in preventing the tethered head from rebinding to the rear binding site, even after ATP-induced isomerization, especially under hindering load. Future studies are required to experimentally verify these models and gain a better understanding of how neck linker tension controls chemical and mechanical transitions of kinesin-1 during hand-over-hand motion. Additionally, studies are needed to examine whether this mechanism extends to other kinesin subfamilies with different neck linker properties, such as varying neck linker lengths (kinesin-2: Hariharan and Hancock, 2009; kinesin-3: Benoit et al., 2024) or unique interactions with the motor domain (kinesin-6: Guan et al., 2016; Ranaivoson et al., 2023).

508 **Materials and Methods**

509 **DNA cloning and protein purification**

510 Cysteines (S43C, E215C, T328C) or mutation in the switch II loop (G234A or G234V)
511 were introduced into a "cysteine-light" human ubiquitous kinesin-1 349-residure
512 monomer with C-terminal His_6 tag (K349CLM), 336-residure monomer with N-
513 terminal His_6 tag (K336CLM), or 490-residue heterodimer with C-terminal His_6 tag and
514 Strep-tag (Rice et al., 1999; Tomishige et al., 2006; Mori et al., 2007). For the neck
515 linker mutations, poly-glycine residues were inserted between L335 and T336 residues
516 (Isojima et al., 2016), by PCR cloning.

517 Monomers and heterodimers were purified as described previously (Tomishige et
518 al, 2000; Tomishige et al., 2006). For crystallization of nucleotide-free kinesin,
519 K336CLM with G234A or G234V mutation was purified as described (Tomishige and
520 Vale, 2000) and the elution from Ni-NTA resin was diluted in the buffer containing
521 20% (w/v) sucrose, 1 mM DTT, and 50 U/ml apyrase (Sigma-Aldrich). Then, the
522 purified kinesin supplemented with apyrase was dialyzed against 25 mM PIPES (pH
523 7.0), 100 mM NaCl, 1 mM EGTA, 2 mM $MgCl_2$ and 1 mM DTT for 1-2 hours to
524 remove nucleotides in the solution, and further incubated with apyrase for 12-16 hours
525 at 4ºC to hydrolyze residual ATP and ADP. The sample was then purified using
526 MonoQ column as described (Case et al, 1997; Tomishige and Vale, 2000), except that
527 buffers without ATP were used and the column was equilibrated with 25 mM PIPES
528 (pH 6.8), 1 mM EGTA, 2 mM $MgCl_2$, 1 mM DTT and 50 mM NaCl. For
529 crystallization of ADP-bound kinesin, K349CLM with G234A mutation was used,
530 which was purified as describe above except that dialysis and incubation with apyrase
531 were omitted. For cryo-EM observation, K349CLM was used.

532

533 **Crystallization, data collection and structural determination**

534 Purified proteins with apyrase treatment were concentrated to 3-4 mg/ml in a
535 crystallization buffer (10 mM Mops-NaOH (pH 7.0), 1 mM EGTA, 1 mM $MgCl_2$, 1
536 mM DTT, 50 mM NaCl, and 20 % (w/v) sucrose). Crystallization was carried out at
537 4ºC by the sitting drop vapor diffusion method with a subsequent streak-seeding. Initial
538 crystals were obtained using a G234V mutant kinesin, which was purified with the same

539 procedures with the G234A mutant, under a reservoir solution conditions of 20-21%
540 PEG3350, 100 mM HEPES-NaOH, pH 7.7-8.0, 200 mM ammonium acetate, 3% xylitol
541 (PS1). G234A mutant crystals were grown in the PS1 by streak-seeding method using a
542 crystal of G234V mutant as a crystal seed. Then, G234A crystal for diffraction was
543 obtained by additional streak-seeding using the crystals of G234A as a crystal nuclei, to
544 exclude the contamination of G234V protein in the crystal. For ADP-bound G234A,
545 protein was concentrated to ~15 mg/ml in the crystallization buffer. Crystals were
546 obtained under reservoir solution conditions of 23% PEG3350, 100 mM Bis-Tris pH 5.5
547 at 20ºC. The crystals were transferred into each reservoir solution supplemented with
548 24% glycerol as a cryoprotectant and flash-cooled at 95K. X-ray diffraction data of apo
549 and ADP-bound kinesin were collected on the BL-5A and NW-12 beamlines
550 (wavelength l = 1.00 Å) at the Photon Factory, respectively. All X-ray diffraction data
551 were integrated and scaled using the program XDS (Kabsch, 1993). The unit cell
552 parameters are described in Table 1.
553 The structures were determined by the molecular replacement method using the
554 coordinates of human kinesin-1 ADP-like structure (PDB# 1BG2; Kull et al., 1996) by
555 the program Phaser (McCoy et al., 2007). Each initial model was refined and rebuilt
556 using programs CNS (Brünger et al., 1998) and Coot (Emsley et al., 2010). In the final
557 refinement process, the program Refmac5 (Murshudov et al., 1997) was used. The data
558 collection and refinement statistics are summarized in Table 1. We expect that the
559 relatively high R-factor for nucleotide-free G234A (Table 1) is likely due to the weak
560 electron density (higher disorder) for the α0 and β2a region.
561
562 **Cryo-EM sample preparation, image analysis and model building**
563 For high resolution cryo-EM observation, frozen grids of kinesin-decorated
564 microtubules were prepared and imaged as described (Nishida et al., 2020) with some
565 modifications. GMPCPP-microtubule (0.03 mg/ml polymerized in BRB80 (80 mM
566 PIPES, 1 mM EGTA, 2 mM $MgSO_4$)) was decorated with monomer kinesin K349CLM
567 described above (0.2 mg/ml) in BRB80 on glow-discharged, carbon-coated grid
568 (Quantifoil R 1.2/1.3, Cu/Rh, 300 mesh) supplemented apyrase (5 U/ml). Blotting and
569 vitrifying were done using Vitrobot (Thermo Fisher Scientific). Cryo-EM data were
570 acquired on a 200-KeV Talos Arctica electron microscope (Thermo Fisher Scientific).

571 Data collection was done as described (Nishida et al., 2020). A total of 2,224 movie
572 stacks were recorded. Image of helical 14-protofilament microtubules were processed
573 with Relion-3 (Zivanov et al., 2018), PyFilamentPicker (Nishida et al., 2020) and
574 Frealign (Grigorieff, 2007), as described (Nishida et al., 2020), except that the CTF
575 parameters were estimated by CTFFIND 4 (Rohou and Grigorieff, 2015). After 3
576 cycles of pseudo-helical refinements, 74,859 particles (8 nm repeat of microtubule)
577 were selected for several cycles of 3D auto-refinement followed by CTF refinement and
578 Bayesian polishing in Relion-3. In total, data representing ~1,050,000 asymmetric units
579 from 2,438 microtubules were averaged. The overall gold-standard resolution was 3.48
580 Å. The local resolution was calculated with MonoRes (Vilas et al., 2018) and the
581 output resolution map was used for local sharpening with LocalDeblur (Ramírez-
582 Aportela et al., 2020).
583 To develop an atomic model for kinesin-microtubule complex, the atomic
584 structure of tubulin (PDB# 3JAT; Zhang et al., 2015) and our G234A apo crystal
585 structure were fit in the sharpened map using UCSF chimera (Pettersen et al., 2004).
586 For model refinement, we used the MDFF package (Trabuco et al., 2008) as described
587 (Nishida et al., 2020), and PHENIX (Adams et al., 2010). Refined model was used for
588 further sharpening of maps with LocScale (Jakobi et al., 2017).
589
590 **Cryo-EM sample preparation, image analysis for gold-labeled kinesin**
591 For gold-cluster labeling, purified K349CLM with T328C mutation was labeled with
592 monomaleimide-undecagold as described (Kikkawa et al., 2000). Free gold-cluster and
593 unlabeled kinesin were removed through RESOURCE S column (1 ml, GE Healthcare)
594 chromatography. The efficiency of labeling was ~80% as estimated using SDS-PAGE.
595 The eluted fraction of the gold-labeled protein was concentrated with Microcon-YM-3
596 (Millipore), and then dialyzed against a BRB12 solution (12 mM PIPES (pH6.8), 1 mM
597 EGTA and 2 mM $MgCl_2$) using micro-dialysis device with 10k MWCO dialysis
598 membrane (Spectrum Laboratories) for 1 hr immediately before the EM preparation.
599 Frozen grids of gold-labeled kinesin-decorated microtubules were prepared and
600 imaged as described (Kikkawa et al., 2000) with some modifications. Microtubule (0.8
601 mg/ml) was decorated with gold-labeled kinesin heads (0.6 mg/ml) in BRB12 buffer
602 supplemented 20 mM taxol and apyrase (5-10 U/ml). Cryo-EM images were recorded

603 with a JEM-3000SFF electron microscope (JEOL Ltd., Tokyo, Japan) equipped with a
604 field emission gun and a super-fluid helium stage (Fujiyoshi et al., 1991) and operated
605 at 300 kV. Images were recorded on SO-163 (Kodak, USA) at a nominal magnification
606 of 40,000x, using a 2-second exposure and a total electron dose of 20 electrons /
607 $Å^2$. The micrographs were developed for 14 min at 20ºC using full-strength D19
608 developer. Selected films were digitized at a step size of 10 μm with a CCD film
609 scanner LeafScan 45 (Scitex), which corresponds to 2.5 Å on the samples.
610 Cryo-EM images were processed with a script system, Ruby-Helix (Metlagel et
611 al., 2007). Images of helical 15-protofilament microtubules were analyzed as
612 described. In total, data representing ~9,000 asymmetric units in 33 segments from four
613 microtubules were averaged.
614
615 **Principal component analysis (PCA) of kinesin structures**
616 PCA of kinesin structures were performed on Bio3D package as described (Grant et al.,
617 2007). Atomic coordinates for kinesin superfamily crystal structures (247 motor
618 domain chains extracted from 137 structures (until PDB# 6G6Z) deposited in PDB plus
619 our G234A and G234V apo crystal structures and cryo-EM apo structure were used.
620 Prior to the PCA, structures were superposed on the invariant "core" residues consisting
621 of 31 residues (see Fig. 3 C, colored in gray; residues 10-15, 48-49, 80-85, 228-231,
622 297-303, 311-316, which are part of structural elements β1, β2, β3, β7, β8 and α6).
623 Subdomains that are invariant in the semi-open, open and closed states were
624 identified with the program GeoStas (Romanowska et al., 2012), using PDB# 5LT1
625 (Cao et al., 2017) as semi-open state, our EM-apo structure as open and PDB# 4HNA as
626 closed states.
627
628 **Modeling of kinesin-tubulin complex for semi-open and closed states**
629 Kinesin-tubulin complex structures were constructed by fitting crystal structures on the
630 cryo-EM maps by UCSF Chimera. The crystal structures of semi-open (PDB# 5TL1;
631 Cao et al., 2017), and closed (#4HNA; Grant et al., 2013) kinesin-1 along with the
632 tubulin dimer model from our cryo-EM-apo structure were fit to the cryo-EM density
633 map of ADP-bound (EMD-5164) and ADP-AlF_x bound (EMD-6188) kinesin-tubulin
634 complex (Sindelar and Downing, 2010; Shang et al., 2014).

635

636 **Modeling of dimeric kinesin and refinement using molecular dynamic simulation**

637 For dimeric kinesin models, two kinesin head-tubulin complexes created as described
638 above were fitted to adjacent tubulin-dimer portions within single protofilament of the
639 cryo-EM density map (EMD-1340; Sindelar and Downing, 2007). The coordinates for
640 the disordered neck linker region and neck coiled-coil were modeled based on those of
641 dimeric kinesin (PDB#3KIN; Kozielski et al., 1997) and loop modeling by satisfaction
642 of spatial restraints were performed using MODELLER program (Fiser et al., 2000).
643 Then MD simulations were applied to the manually modeled neck linker to refine the
644 positions of the disordered neck linker region. The MD calculation refines the neck
645 linker configuration but does not significantly affect the end-to-end distance of the neck
646 linker.

647 The MD simulations of the disordered neck linker were performed by
648 GROMACS 4.0.2 (Berendsen et al., 1995; Lindahl et al., 2001) with the AMBER-99SB
649 for proteins (Lindahl et al., 2001; Sorin and Pande, 2005; DePaul et al., 2010) and the
650 TIP3P for waters. The simulation system contained the disordered neck linker, neck
651 coiled-coil, all the atoms of the kinesin motor domain and tubulin within 12 Å from the
652 neck linker, and a few additional residues for continuity, which was solvated with
653 waters and counter ions in a box with water layers at least 9 Å from the protein. The
654 position restraints were applied to all the non-H atoms except the disordered neck linker
655 and the neck coiled-coil, and to the main chain atoms at the boundary residues between
656 the head and the neck-linker; K323 residue in the leading head and E334 (T_{closed}) or
657 K323 residue (T_{open}) in the trailing head. To inhibit unzipping of the coiled-coil, we
658 added a harmonic potential between the Cα atoms of the residue 337 in both
659 chains. All the systems were first energy-minimized and waters and ions were then
660 equilibrated for 1 ns. The production runs were performed for 30 ns for T_{closed}-L_{open}, 20
661 ns for T_{closed}-L_{closed}, 16 ns for T_{open}-L_{open}, and 30 ns for T_{open}-L_{closed}, in which the
662 coordinates were saved every 2ps (every 1ps for the T_{open}-L_{open} state). The simulations
663 employed the NPT ensemble (Parrinello and Rahman, 1981; Berendsen et al., 1984)
664 with 300 K and 1 bar, the periodic boundary conditions, the particle mesh Ewald
665 (Darden et al., 1993) with cut-off 1.0 nm for the electrostatics, the van der Waals cutoff
666 1.4 nm, the LINCS for constraining bond lengths (Hess et al., 1997), and 1 fs and 2 fs

667 time step in the production run for the T_{open}-L_{open} and for the others, respectively. For
668 each simulation, convergence was assessed by a few measures.
669
670 **Estimation of the tension applied to the neck linker**
671 The MD simulations for the estimation of tension posed to the disordered neck linker in
672 the refined dimer models were performed by GROMACS 4.5.5 with the AMBER-99SB
673 for proteins and the TIP3P for waters. The simulation system contained the neck
674 coiled-coil and the disordered neck linker region of which two ends are E334 for T_{closed}
675 or T328 residue for T_{open} in the trailing head and I325 residue in the leading head
676 (Figure S4 D). These protein segments were solvated with waters and counter ions in a
677 box with water layers at least 15 Å from the protein. The initial structures were taken
678 from the refinement structures shown in Fig. 6. To evaluate the tension applied to the
679 neck linker in each conditions, the distance constraints were applied to the Cα atoms of
680 the edge residues in both ends of the neck-linker in the form of harmonic potential: $k (R$
681 $- R_0)^2$, where R is the distance between Cα atoms on two ends, spring-constant k is set
682 as 105 kJ/mol/nm^2, constraint distance R_0 is set as the corresponding average distance
683 for each system during the refinement MD. To inhibit unwinding of the neck coiled-
684 coil, we added a harmonic potential between the Cα atoms of the residue 337 in the two
685 polypeptides as described above. Starting from the refined structures, all the systems
686 were first energy-minimized and waters and ions were then equilibrated for 1ns. The
687 production runs for estimation of the tension were performed for 200 ns for T_{closed}-L_{open},
688 and 100 ns for the other systems, in which the deviation of the distance from the
689 constraint distance R_0 were saved every 0.2 ps. The neck linker tension was calculated
690 as the spring constant k multiplied by the deviation from the constraint distance R_0.
691 Other simulation protocols are the same as those described in the refinement-MD. For
692 each system, convergence of the tension was confirmed (see Fig. 7 A).
693
694 **Single-molecule FRET observations**
695 Single molecule FRET measurement and data analysis were carried out as described
696 previously (Tomishige et al., 2006; Mori et al., 2007) using Cy3- and Cy5-labeled
697 heterodimers (E215C in one chain and S43C in the other chain) with insertions of poly-

698 Gly between L335 and T336 residues. Dual-labeled heterodimer molecules bound to the
699 axoneme in the presence of 0.2-10 μM ADP and 5 U/ml hexokinase (which converts
700 contaminating ATP to ADP) were excited with 514 nm argon laser (35LAP321; Melles
701 Griot), and donor and acceptor fluorophores were simultaneously observed using a
702 Dual-View (Optical Insights) and EM-CCD camera (iXon DV860; Andor) at an
703 acquisition rate of 100 frames/s.

704

Online supplemental material

Supplemental data and legends relating to Figs. 1, 2, 6, and 7 can be found in Figs S1, S2, S3, S4, and S5.

Data availability

The data that support the findings of this study are available from the corresponding author upon request. The atomic coordinates and structure factors for the crystal structures have been deposited in the Protein Data Bank under the accession codes 9L6K (nucleotide-free G234V mutant), 9L78 (nucleotide-free G234A mutant), and 9L7E (ADP-bound G234A mutant). The cryo-EM density map has been deposited in the Electron Microscopy Data Bank under accession code EMD-62874, and the corresponding atomic coordinates have been deposited in the Protein Data Bank under accession code 9L7M.

Acknowledgments

We thank M. Nakajima for assistance in the cloning of constructs, C. Sindelar for providing cryo-EM density maps, Y. Fujiyoshi for use of cryo-EM microscope for gold-labeled kinesin, R. Vale for helpful discussions. The synchrotron-radiation experiments were performed at the Photon Factory (2003S2-002 and 2008S2-001).

M. Tomishige, M. Kikkawa and T. Makino are supported by Research Grant for Young Investigators from Human Frontier Science Program. M. Tomishige is supported by Grants-in-Aid for Scientific Research on Priority Areas from MEXT, and by the Asahi Glass Foundation. M. Tanokura is supported by the National Project on Protein Structural and Functional Analyses and the Targeted Proteins Research Program of MEXT.

Author contributions: M. Tomishige and T. Makino conceived and designed the experiments. T. Makino carried out purification, crystallization, structural determination and analysis with K. Miyazono and M. Tanokura. T. Makino and M. Kikkawa performed cryo-EM observation and analysis with Y. Komori and H. Yanagisawa. R. Kanada and S. Takada ran MD simulations. T. Mori and M. Tomishige carried out smFRET observations. T. Makino, R. Kanada and T. Mori prepared figures and M. Tomishige wrote the manuscript.

Disclosures: The authors declare no competing interests exist.

References

Adams, P. D. et al. 2010. PHENIX: A comprehensive Python-based system for macromolecular structure solution. *Acta Crystallogr. Sect. D Biol. Crystallogr.* 66:213–221.

Andreasson, J.O.L., B. Milic, G-Y. Chen, N.R. Guydosh, W.O. Hancock, and S.M. Block. 2015. Examining kinesin processivity within a general gating framework. *Elife.* 4:e07403.

Atherton, J. et al. Conserved mechanisms of microtubule-stimulated ADP release, ATP binding, and force generation in transport kinesins. *Elife* **3**, e03680 (2014).

Asbury, C.L., A.N. Fehr, and S.M. Block. 2003. Kinesin moves by an asymmetric hand-over-hand mechanism. *Science*. 302:2130-2134.

Asenjo, A.B., and H. Sosa. 2009. A mobile kinesin-head intermediate during the ATP-waiting state. *Proc. Natl. Acad. Sci. USA*. 106:5657–5662.

Benoit M.P.M.H. et al. 2021. Structural basis of mechano-chemical coupling by the mitotic kinesin KIF14. *Nat. Commun.* 12:3637.

Benoit, M.P.M.H., B. Hunter, J.S. Allingham, and H. Sosa. 2023. New insights into the mechanochemical coupling mechanism of kinesin-microtubule complexes from their high-resolution structures. *Biochem. Soc. Trans.* 51:1505-1520.

Benoit, M.P.M.H. et al. 2024. Cryo-EM unveils kinesin KIF1A's processivity mechanism and the impact of its pathogenic variant P305L. *Nat. Commun.* 15:4430.

Berendsen, H.J.C., J.P.M. Postma, W.F. van Gunsteren, A. DiNola, and J.R. Haak. 1984. Molecular dynamics with coupling to an external bath. *J. Chem. Phys.* 81:3684–3690.

Berendsen, H.J.C., D. van der Spoel, and R. van Drunen. 1995. GROMACS: A message-passing parallel molecular dynamics implementation. *Comput. Phys. Commun.* 91:43–56.

Block, S.M. 2007. Kinesin motor mechanics: binding, stepping, tracking, gating, and limping. *Biophys. J.* 92:2986-2995.

Brünger, A.T. et al. 1998. Crystallography & NMR system: A new software suite for macromolecular structure determination. *Acta Crystallogr. D. Biol. Crystallogr.* 54:905–921.

Cao, L. et al. 2014. The structure of apo-kinesin bound to tubulin links the nucleotide

770 cycle to movement. *Nat. Commun.* 5:5364.
771 Cao, L., S. Cantos-Fernandes, and B. Gigant. 2017. The structural switch of nucleotide-
772 free kinesin. *Sci. Rep.* 7:42558.
773 Case, R.B., D.W. Pierce, N. Hom-Booher, C.L. Hart, and R.D. Vale. 1997. The
774 Directional Preference of Kinesin Motors Is Specified by an Element outside of the
775 Motor Catalytic Domain. *Cell.* 90:959–966.
776 Clancy, B.E., W.M. Behnke-Parks, J.O.L. Andreasson, S.S. Rosenfeld, and S.M. Block.
777 2011. A universal pathway for kinesin stepping. *Nat. Struct. Mol. Biol.* 18:1020–
778 1027.
779 Cross, R.A. 2004. The kinetic mechanism of kinesin. *Trends Biochem. Sci.* 29:301–309.
780 Cochran, J.C. 2015. Kinesin motor enzymology: chemistry, structure, and physics of
781 nanoscale molecular machines. *Biophys. Rev.* 7:269-299.
782 Darden, T., D. York, and L. Pedersen. 1993. Particle mesh Ewald: An N·log(N) method
783 for Ewald sums in large systems. *J. Chem. Phys.* 98:10089–10092.
784 DePaul, A.J., E.J. Thompson, S.S. Patel, K. Haldeman, and E.J. Sorin. 2010. Equilibrium
785 conformational dynamics in an RNA tetraloop from massively parallel molecular
786 dynamics. *Nucleic Acids Res.* 38:4856–4867.
787 Emsley, P., B. Lohkamp, W.G. Scott, and K. Cowtan. 2010. Features and development
788 of Coot. *Acta Crystallogr. D. Biol. Crystallogr.* 66:486–501.
789 Fiser, A., R.K. Do, A. Sali. 2000. Modeling of loops in protein structures. *Protein Sci.*
790 9:1753–1773.
791 Fujiyoshi, Y. et al. 1991. Development of a superfluid helium stage for high-resolution
792 electron microscopy. *Ultramicroscopy.* 38:241–251.
793 Gennerich, A., and R.D. Vale. 2009. Walking the walk: how kinesin and dynein
794 coordinate their steps. *Curr. Opin. Cell Biol.* 21:59–67.
795 Gigant, B. et al. 2013. Structure of a kinesin-tubulin complex and implications for
796 kinesin motility. *Nat. Struct. Mol. Biol.* 20:1001–1007.
797 Grant, B.J., J.A. McCammon, L.S.D. Caves, and R.A. Cross. 2007. Multivariate
798 analysis of conserved sequence-structure relationships in kinesins: coupling of the
799 active site and a tubulin-binding sub-domain. *J. Mol. Biol.* 368:1231–1248.
800 Grigorieff, N. 2007. FREALIGN: High-resolution refinement of single particle structures.
801 *J. Struct. Biol.* 157:117–125.

802 Guan, R. et al. 2017. Crystal structure of Zen4 in the apo state reveals a missing
803 conformation of kinesin. *Nat. Commun.* 8:14951.
804 Guydosh, N.R., and S.M. Block. 2009. Direct observation of the binding state of the
805 kinesin head to the microtubule. *Nature*. 461:125–128.
806 Hackney, D.D. 1994. Evidence for alternating head catalysis by kinesin during
807 microtubule-stimulated ATP hydrolysis. *Proc. Natl. Acad. Sci. USA.* 91:6865–6869.
808 Hackney, D.D., M.F. Stock, J. Moore, and R.A. Patterson. 2003. Modulation of kinesin
809 half-site ADP release and kinetic processivity by a spacer between the head groups.
810 *Biochemistry*. 42:12011–12018.
811 Hancock, W.O., and J. Howard. 1999. Kinesin's processivity results from mechanical
812 and chemical coordination between the ATP hydrolysis cycles of the two motor
813 domains. *Proc. Natl. Acad. Sci. USA*. 96:13147-13152.
814 Hariharan, V., and W. O.Hancock. 2009. Insights into the Mechanical Properties of the
815 Kinesin Neck Linker Domain from Sequence Analysis and Molecular Dynamics
816 Simulations. *Cell. Mol. Bioeng.* 2:177–189.
817 Hess, B., H. Bekker, H.J.C. Berendsen, and J.G.E.M. Fraaije. 1997. LINCS: A linear
818 constraint solver for molecular simulations. *J. Comput. Chem.* 18:1463–1472.
819 Isojima, H., R. Iino, Y. Niitani, H. Noji, and M. Tomishige. 2016. Direct observation of
820 intermediate states during the stepping motion of kinesin-1. *Nat. Chem. Biol.*
821 12:290–297.
822 Jakobi, A.J., M. Wilmanns, and C. Sachse. 2017. Model-based local density sharpening
823 of cryo-EM maps. *Elife.* 6:e27131.
824 Kabsch, W. 1993. Automatic processing of rotation diffraction data from crystals of
825 initially unknown symmetry and cell constants. *J. Appl. Crystallogr.* 26:795–800.
826 Kaseda, K., H. Higuchi, and K. Hirose. 2003. Alternate fast and slow stepping of a
827 heterodimeric kinesin molecule. *Nat. Cell Biol.* 5:1079-1082.
828 Kikkawa, M., Y. Okada, and N. Hirokawa. 2000. 15 Å resolution model of the
829 monomeric kinesin motor, KIF1A. *Cell*. 100:241–252.
830 Kozielski, F. et al. 1997. The crystal structure of dimeric kinesin and implications for
831 microtubule-dependent motility. *Cell.* 91:985–994.
832 Kull, F.J., E.P. Sablin, R. Lau, R.J. Fletterick, R.D. Vale. 1996. Crystal structure of the
833 kinesin motor domain reveals a structural similarity to myosin. *Nature*. 380:550–555.

Lindahl, E., B. Hess, and D. van der Spoel. 2001. GROMACS 3.0: a package for molecular simulation and trajectory analysis. *J. Mol. Model.* 7:306–317.

McCoy, A.J. et al. 2007. Phaser crystallographic software. *J. Appl. Crystallogr.* 40:658–674.

Metlagel, Z., Y.S. Kikkawa, M. Kikkawa. 2007. Ruby-Helix: an implementation of helical image processing based on object-oriented scripting language. *J. Struct. Biol.* 157:95–105.

Mori, T., R.D. Vale, and M. Tomishige. 2007. How kinesin waits between steps. *Nature*. 450:750–754.

Morikawa, M. et al. 2015. X-ray and cryo-EM structures reveal mutual conformational changes of kinesin and GTP-state microtubules upon binding. *EMBO J.* 34:1270.

Murshudov, G.N., A.A. Vagin, and E.J. Dodson. 1997. Refinement of macromolecular structures by the maximum-likelihood method. *Acta Crystallogr. D. Biol. Crystallogr.* 53:240–255.

Niitani, Y., K. Matsuzaki, E. Jonsson, R.D. Vale, and M. Tomishige. 2024. Kinetic regulation of kinesin's two motor domains coordinates its stepping along microtubules. *bioRxiv* ???.

Nishida, N. et al. 2020. Structural basis for two-way communication between dynein and microtubules. *Nat. Commun.* 11:1–8.

Parke, C.L., E.J. Wojcik, S. Kim, and D.K. Worthylake. 2010. ATP hydrolysis in Eg5 kinesin involves a catalytic two-water mechanism. *J. Biol. Chem.* 285:5859-5867.

Parrinello, M., and A. Rahman. 1981. Polymorphic transitions in single crystals: A new molecular dynamics method. *J. Appl. Phys.* 52:7182–7190.

Pettersen, E.F. et al. 2004. UCSF Chimera—A visualization system for exploratory research and analysis. *J. Comput. Chem.* 25:1605–1612.

Ramírez-Aportela, E. et al. 2020. Automatic local resolution-based sharpening of cryo-EM maps. *Bioinformatics.* 36:765–772.

Ranaivoson, F.M. et al. 2023. Nucleotide-free structures of KIF20A illuminate atypical mechanochemistry in this kinesin-6. *Open Biol*. 13:230122.

Rice, S. et al. 1999. A structural change in the kinesin motor protein that drives motility. *Nature*. 402:778–784.

Rice S. et al., 2003. Thermodynamic properties of the kinesin neck-region docking to

866 the catalytic core. *Biophys. J.* 84:1844-1854.
867 Rohou, A., and N. Grigorieff. 2015. CTFFIND4: Fast and accurate defocus estimation
868 from electron micrographs. *J. Struct. Biol.* 192:216–221.
869 Romanowska, J., K.S. Nowiński, and J. Trylska. 2012. Determining geometrically stable
870 domains in molecular conformation sets. *J. Chem. Theory Comput.* 8:2588–2599.
871 Scarabelli, G., and B.J. Grant. 2013. Mapping the structural and dynamical features of
872 kinesin motor domains. *PLoS Comput. Biol.* 9:e1003329.
873 Schief, W.R., R.H. Clark, A.H. Crevenna, and J. Howard. 2004. Inhibition of kinesin
874 motility by ADP and phosphate supports a hand-over-hand mechanism. *Proc. Natl.*
875 *Acad. Sci. USA*. 101:1183-1188.
876 Shang, Z. et al. 2014. High-resolution structures of kinesin on microtubules provide a
877 basis for nucleotide-gated force-generation. *Elife*. 3:e04686.
878 Shastry, S. and W. O. Hancock. 2010. Neck linker length determines the degree of
879 processivity in kinesin-1 and kinesin-2 motors. *Curr. Biol.* 20:939-943.
880 Shipley, K. et al. 2004. Structure of a kinesin microtubule depolymerization machine.
881 *EMBO J.* 23:1422.
882 Sindelar, C.V., and K.H. Downing. 2007. The beginning of kinesin's force-generating
883 cycle visualized at 9-Å resolution. *J. Cell Biol.* 177:377–385.
884 Sindelar, C.V., and K.H. Downing. 2010. An atomic-level mechanism for activation of
885 the kinesin molecular motors. *Proc. Natl. Acad. Sci. USA.* 107:4111–4116.
886 Sindelar, C.V. 2011. A seesaw model for intermolecular gating in the kinesin motor
887 protein. *Biophys. Rev.* 3:85-100.
888 Sorin, E.J., and V.S. Pande. 2005. Exploring the helix-coil transition via all-atom
889 equilibrium ensemble simulations. *Biophys. J.* 88:2472–2493.
890 Taniguchi, Y., M. Nishiyama, Y. Ishii, and T. Yanagida. 2005. Entropy rectifies the
891 brownian steps of kinesin. *Nat. Chem. Biol.* 1:342.
892 Tomishige, M., and R.D. Vale. 2000. Controlling kinesin by reversible disulfide cross-
893 linking: Identifying the motility-producing conformational change. *J. Cell Biol.*
894 151:1081–1092.
895 Tomishige, M., N. Stuurman, and R.D. Vale. 2006. Single-molecule observations of
896 neck linker conformational changes in the kinesin motor protein. *Nat. Struct. Mol.*
897 *Biol.* 13:887–894.

Trabuco, L.G., E. Villa, K. Mitra, J. Frank, and K. Schulten. 2008. Flexible Fitting of Atomic Structures into Electron Microscopy Maps Using Molecular Dynamics. *Structure* 16:673–683.

Vale, R.D., R.A. Milligan. 2000. The way things move: looking under the hood of molecular motor proteins. *Science*. 288:88–95.

Vale, R.D. 2003. The molecular motor toolbox for intracellular transport. *Cell*. 112:467-480.

Valentine, M.T., and S.P. Gilbert. 2007. To step or not to step? How biochemistry and mechanics influence processivity in kinesin and Eg5. *Curr. Opin. Cell Biol.* 19:75-81.

Vilas, J. L. et al. 2018. MonoRes: automatic and accurate estimation of local resolution for electron microscopy maps. *Structure.* 26:337-344.

Wolff, J.O. et al. 2023. MINFLUX dissects the unimpeded walking of kinesin-1. *Science*. 379:1004-1010.

Yildiz, A., M. Tomishige, R.D. Vale, and P.R. Selvin. 2004. Kinesin walks hand-over-hand. *Science*. 303:676–678.

Yildiz, A., M. Tomishige, A. Gennerich, and R.D. Vale. 2008. Intramolecular strain coordinates kinesin stepping behavior along microtubules. *Cell*. 134:1030–1041.

Zhang, R., G.M. Alushin, A. Brown, and E. Nogales. 2015. Mechanistic origin of microtubule dynamic instability and its modulation by EB proteins. *Cell.* 162:849–859.

Zivanov, J. et al. 2018. New tools for automated high-resolution cryo-EM structure determination in RELION-3. *Elife.* 7:e42166.

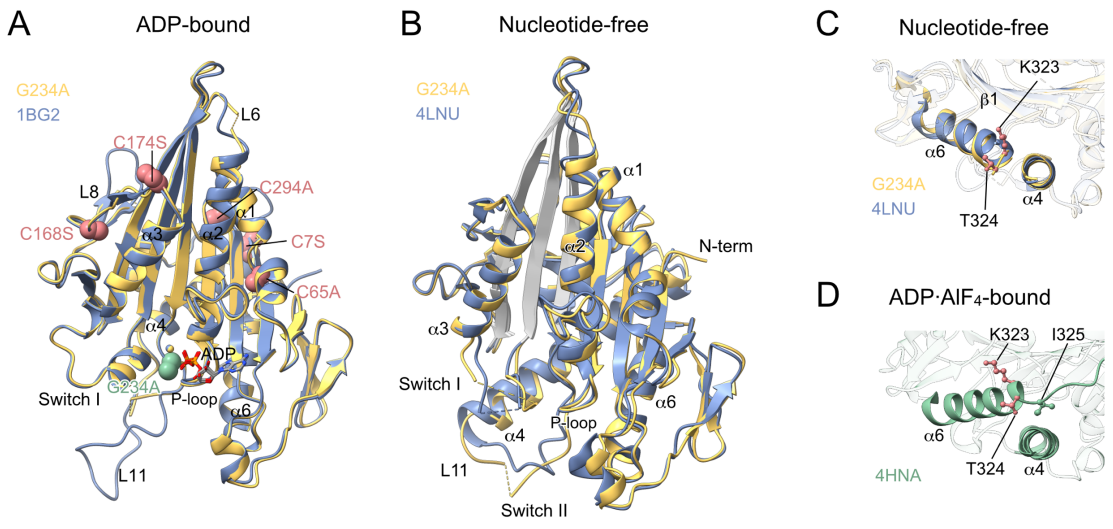

Figure 1. **Crystal structures of G234A mutant kinesin-1 motor domain. (A)** 2.4 Å crystal structure of Cys-light mutant kinesin-1 (336 amino-acids) with G234A mutation complexed with ADP (yellow), aligned with the ADP-bound structure of wild-type human kinesin-1 (blue; PDB# 1BG2 (Kull et al., 1996)). The root mean square deviations (RMSD) of backbone atoms between these structures was 0.819 Å. The G234A residue is highlighted as a green sphere, and cysteine substitutions are shown as red spheres. **(B)** 2.8 Å crystal structure of nucleotide-free G234A mutant kinesin-1 motor domain (yellow), aligned with the nucleotide-free motor domain from the kinesin-tubulin complex crystal structure (blue; #4LNU (Cao et al., 2014)). The RMSD of backbone atoms between these structures was 1.259 Å. L11 is disordered in our crystal structure but ordered in 4LNU, suggesting that microtubule binding is necessary for L11 folding. **(C and D)** Close-up views of the α4 and α6 helices in nucleotide-free and ADP·AlF_4-bound (green; #4HNA (Gigant et al., 2013)) states. The initial residues of the neck linker (K323, T324, and I325) are highlighted as ball and stick models.

	G234A (nucleotide-free)	G234A (ADP)	G234V (nucleotide-free)
Data collection			
Space group	$P2_1$	$P2_1$	$P2_1$
Cell dimensions			
a, *b*, *c* (Å)	44.2, 156.9, 53.0*	49.4, 67.9, 55.5	44.1, 162.4, 53.2*
β (°)	114.6	96.1	114.5
Resolution (Å)	20-2.82 (2.82-2.90) #	20-2.40 (2.40-2.46)	20-2.80 (2.87-2.80)
R_{merge}	0.062 (0.098)	0.052 (0.412)	0.051 (0.076)
$I/\sigma I$	16.13 (4.96)	17.90 (3.73)	29.58 (13.25)
Completeness (%)	95.5 (57.5)	99.7 (100)	97.6 (85.6)
Redundancy	3.4 (1.3)	4.2 (4.2)	7.1 (4.6)
Refinement			
Resolution (Å)	19.6-2.82	20-2.40	19.5-2.80
No. reflections	15129	14330	16383
R_{work}/ R_{free} (%)	20.7/ 26.5	19.2/ 25.2	20.0/ 25.8
No. atoms			
Protein	4761	2363	5017
ADP/ion	0/0	27/1	0/0
Water	1	53	0
B-factors (Å^2)			
Protein	24.2	45.0	27.5
ADP/ion		33.6/27.4	
Water	12.1	45.0	
R.m.s deviations			
Bond lengths (Å)	0.004	0.019	0.003
Bond angles (º)	0.61	1.86	0.54

Table 1. **Data collection and refinement statistics of the crystal structures.** *Nucleotide-free G234A and G234V crystal contains two chains in an asymmetric unit. #Numbers in parenthesis show resolution in the highest resolution shell.

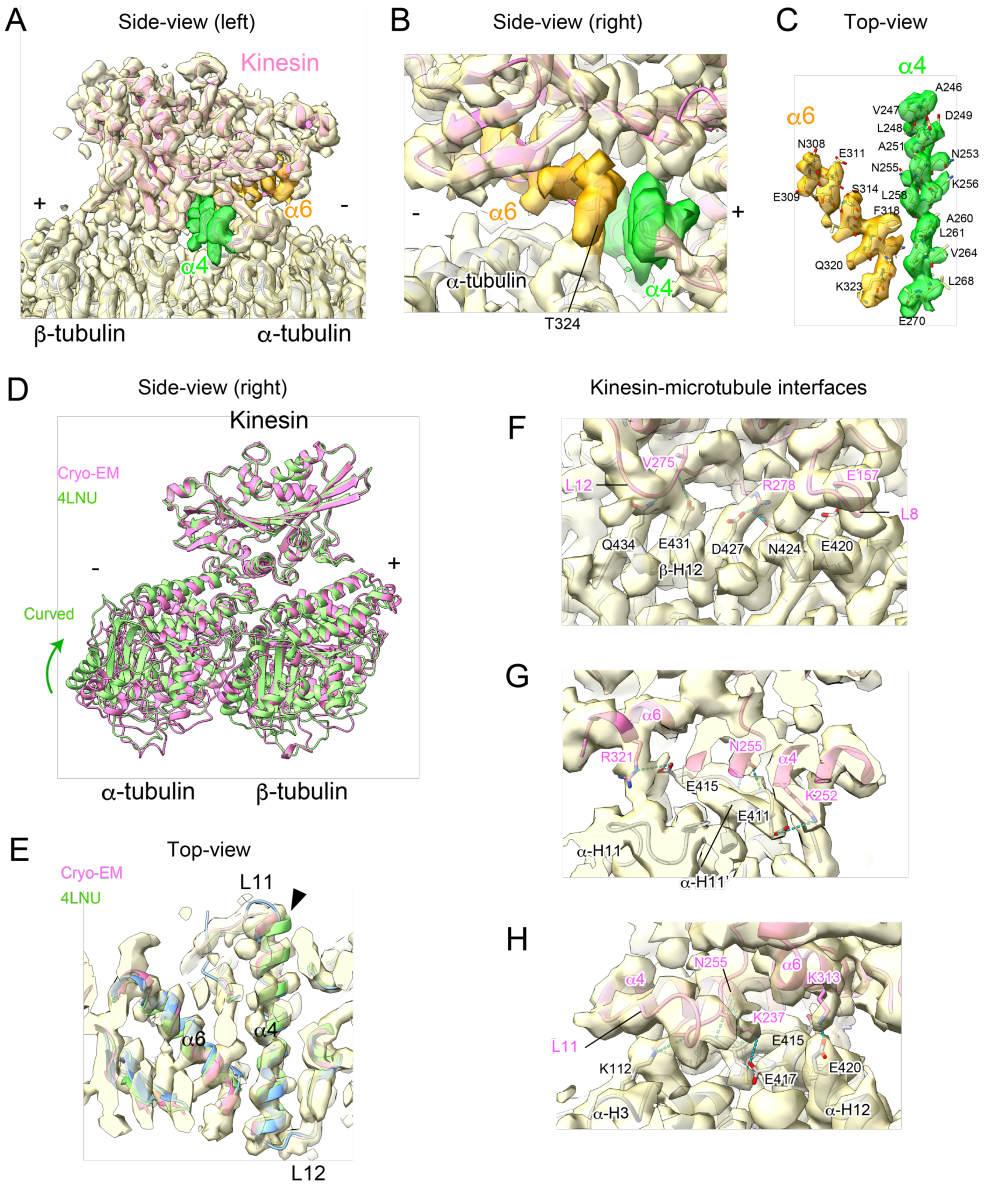

Figure 2. **Cryo-EM density map and atomic model of nucleotide-free kinesin on the microtubule. (A-C)** Cryo-EM reconstructed map of the nucleotide-free kinesin-microtubule complex (light yellow) and its refined atomic model (kinesin; pink, tubulin; gray) are shown in cartoon representation (A and B) and stick representation (C). The cryo-EM map of α4 and α6 helices are highlighted in green and orange, respectively. Panels B and C provide close-up views of α4 and α6. (**D and E**) The atomic model derived from the cryo-EM map was aligned with the previously solved nucleotide-free structure of human kinesin-1 motor domain bound to tubulin-DARPin complex (green; #4LNU (Cao et al., 2014)). These structures were similar except that the N-terminus of α4 of 4LNU deviated from the cryo-EM density map, as shown by the arrowhead in panel E. **(F-H)** Close-up views of the cryo-EM map and its atomic model of the kinesin-microtubule interface. The interface of kinesin with β-tubulin (F) and α-tubulin (G and H) is shown. Hydrogen bonds and salt bridges are marked as blue dashed lines.

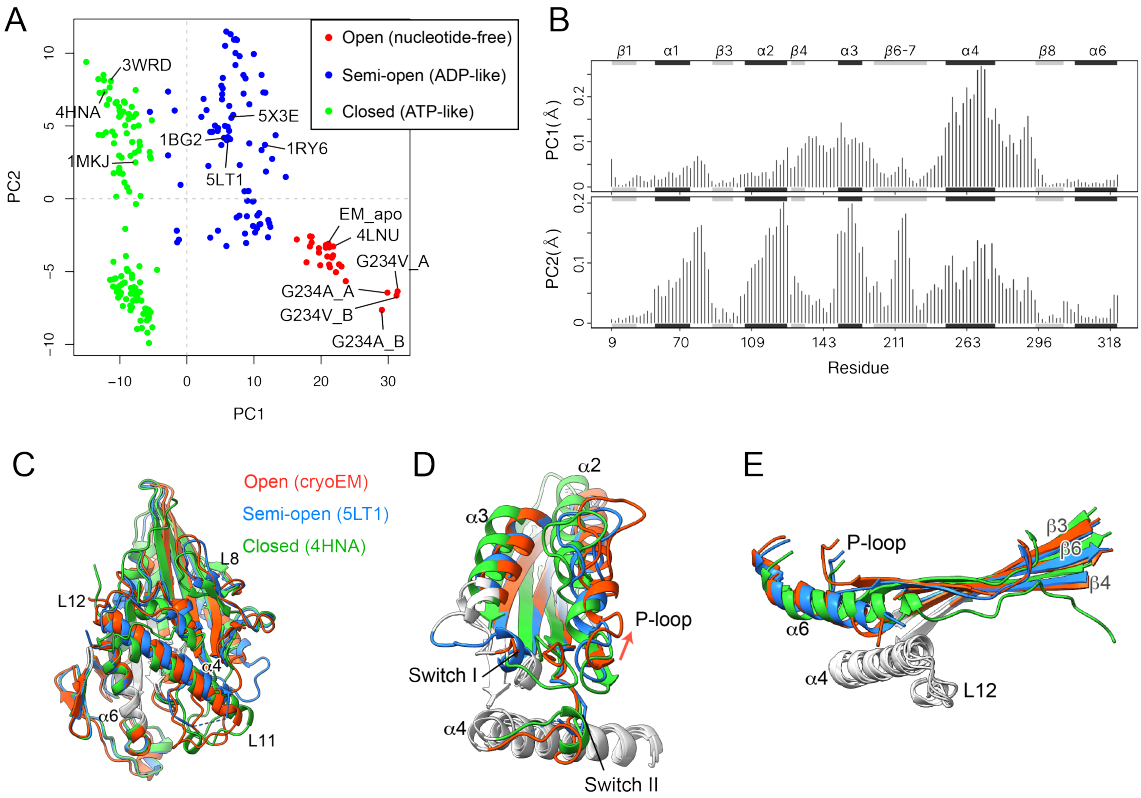

Figure 3. **Structural classification of kinesin motor domain using PCA. (A)** Principal component analysis (PCA) classified kinesin crystal structures based on their conformational similarity. We projected kinesin structures from the Protein Data Bank—including our crystal and cryo-EM apo structure—onto principal planes defined by the two most significant principal components (PC1 and PC2). Each dot's color represents one of three classes obtained from hierarchical clustering of the projected structures in the PC1 to PC4 planes. Representative structures of kinesin-1 for each class (1BG2, 1MKJ, 4HNA, 4LNU) and previously reported nucleotide-free structures (1RY6, 3WRD, 5LT1, 5X3E), are labeled with their PDB code. **(B)** The contribution of each residue (as for human kinesin-1) to the first two principal components (PC1 and PC2). Shaded rectangles indicate the corresponding secondary structures. **(C-E)** Comparison of representative structures from three classes. 5LT1 was chosen to represent the semi-open state, as the N-terminus of its α4 helix extends similarly to the microtubule-bound states (cryoEM apo and 4HNA). These three structures are superposed on the invariant "core" (gray in C) or the B-domain (gray in D and E). These structures were used to identify subdomains (see Fig. 4).

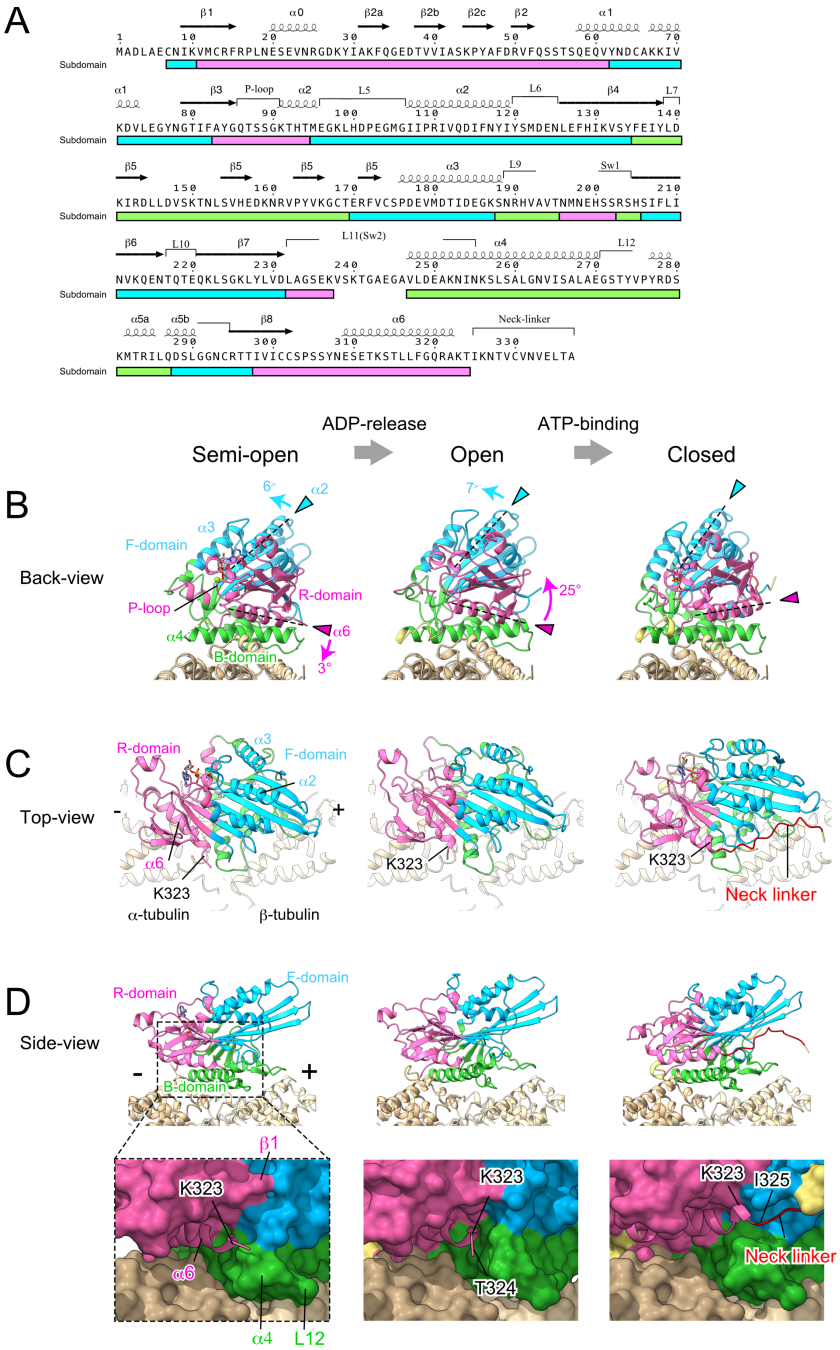

Figure 4. **Subdomain motions associated with the allosteric conformational changes of kinesin motor domain on the microtubule. (A)** The residues classified into three subdomains are colored in magenta (R-domain), cyan (F-domain) and green (B-domain). **(B-D)** Three classes of conformational state of the kinesin motor domain (Fig. 3) bound to the microtubule, colored by subdomain. Unassigned residues, which are disordered in the semi-open state, are yellow and the neck linker is red. The kinesin-microtubule complex models of semi-open and closed states were prepared by fitting 5LT1 and 4HNA onto the cryo-EM density maps of ADP-bound (Sindelar and Downing, 2010) and ADP·AlF_x-bound (Shang et al., 2014) states, respectively. For clarity, we depicted the semi-open state with MgADP bound by incorporating the MgADP from the 1BG2 structure into the 5LT1 (nucleotide-free) structure. The rotational movements of R- and F-domains relative to the microtubule—from semi-open to open and from open to closed—are represented by angular changes in the long axes of α6 and α2 helices (arrowheads), respectively.

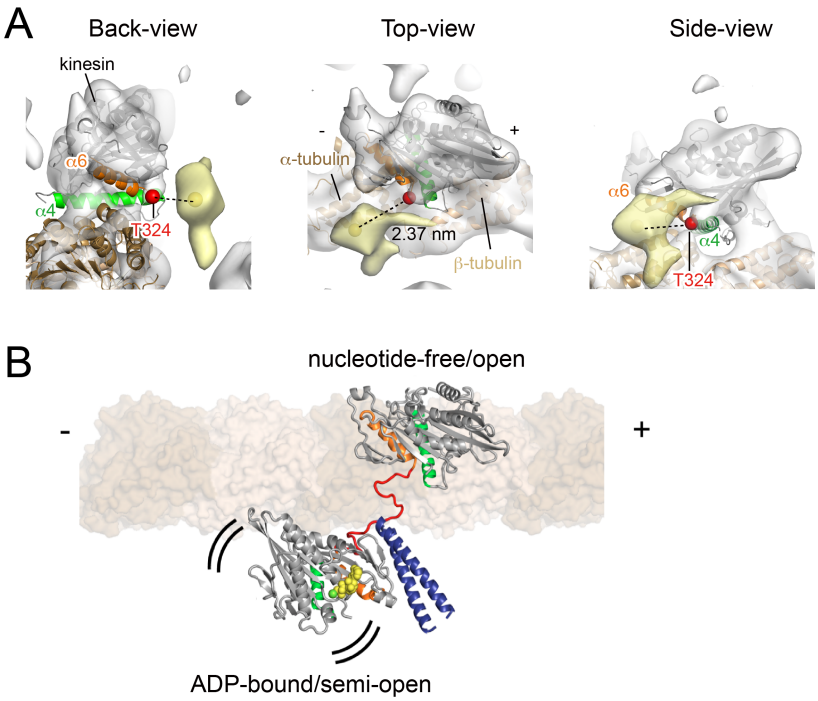

Figure 5. **Cryo-EM observation of the proximal end of the neck linker in the nucleotide-free state. (A)** 15 Å cryo-EM density map (σ =1.0) of gold-labeled kinesin-microtubule complex under nucleotide-free condition. A gold cluster was specifically attached to the Cys328 residue on the neck linker. α4 and α6 helices are shown in green and orange, respectively. Red spheres indicate the last ordered residue of the neck linker in the nucleotide-free state (T324). Nucleotide-free kinesin and tubulin crystal structures have been fit to the density map. Extra density corresponding to the attached gold is highlighted in light yellow. The centroid of the gold cluster, identified as the maximum density region (σ =2.7), is shown as yellow spheres. **(B) S**tructural model of kinesin dimer in the one-head-bound state: the microtubule-bound head is nucleotide-free and in the open state, while the unbound head is in the semi-open state, tethered by disordered neck linkers. The neck linker and the neck coiled-coil are shown in red and blue, respectively.

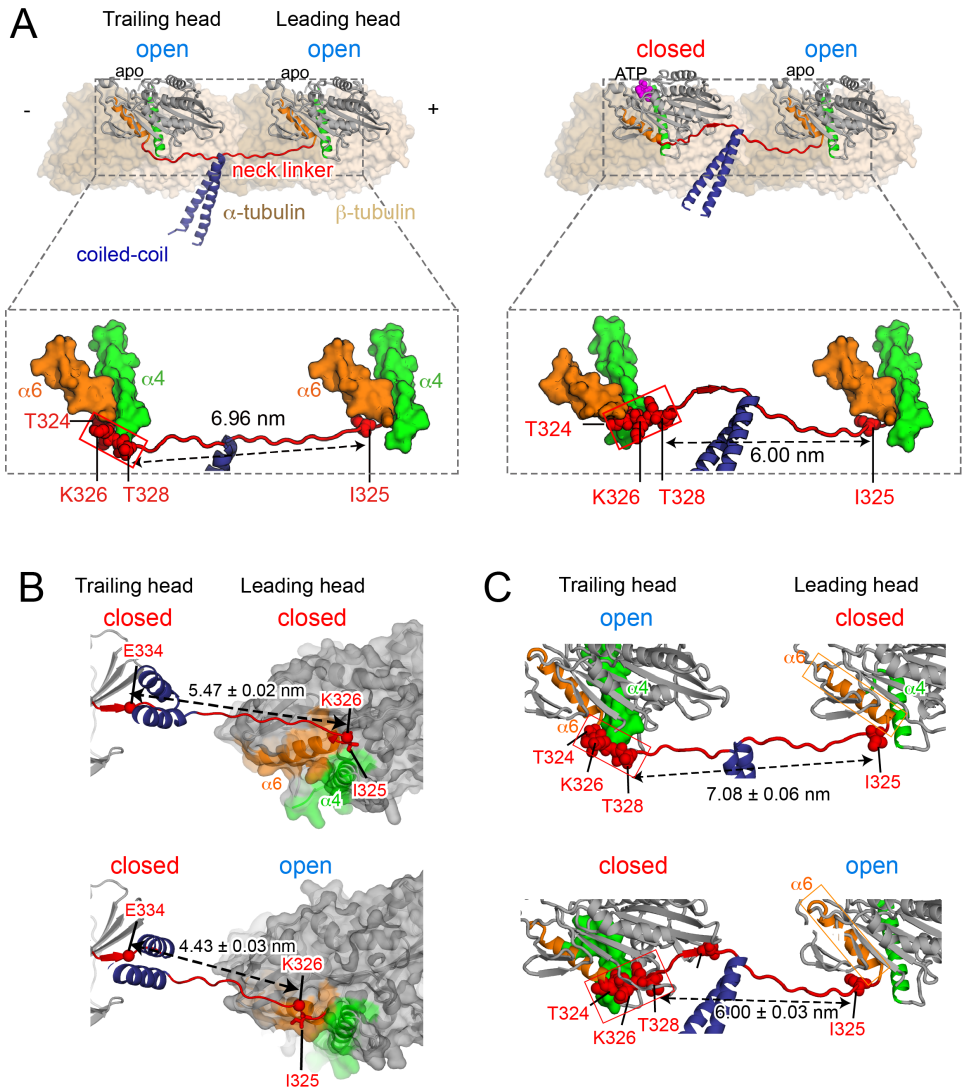

Figure 6. **Structural models of dimeric kinesin on microtubule in all four combinations of open and closed heads. (A)** Atomic models of kinesin dimer on microtubule in the two-head-bound state (top view): one with both heads nucleotide-free and in open state (left; termed T_{open}-L_{open}) and another with the trailing head ATP-bound and in closed state, while the leading head remains the nucleotide-free/open state (right; termed T_{closed}-L_{open}). Thermally equilibrium conformations of the disordered neck linkers were determined by running MD simulations (Fig. S4). The lower panel shows close-ups of the neck linkers (red), α4 (green) and α6 (orange) helices. Numbers indicate the distance between the T328 residue in the trailing head and the I325 residue in the leading head. (**B**) Close-up view (side view) of the atomic model of two-head-bound state with both heads in closed state (upper; T_{closed}-L_{closed}), compared with the T_{closed}-L_{open} model (lower). We modeled the T_{closed}-L_{closed} such that the initial segment of the neck linker (323-325 residues) of the leading head docks onto the head, while the rest remains detached. Even this partial docking leads to a considerable increase in neck linker extension, prohibiting the open-to-closed conformational change of the leading head (Fig. 9, purple rectangle). **(C)** Atomic model of T_{open}-L_{closed} state (upper), compared with the T_{closed}-L_{open} model (lower). This model represents the off-pathway transition where the tethered head binds to the rear-tubulin binding site after ATP-induced isomerization of the microtubule bound head (Fig. 9, green hexagonal box). In this model, the I325 residue of the leading head is detached from the head, but its position is translated toward the plus-end of microtubule due to the rotational movement and extension of the α6 helix (orange rectangle).

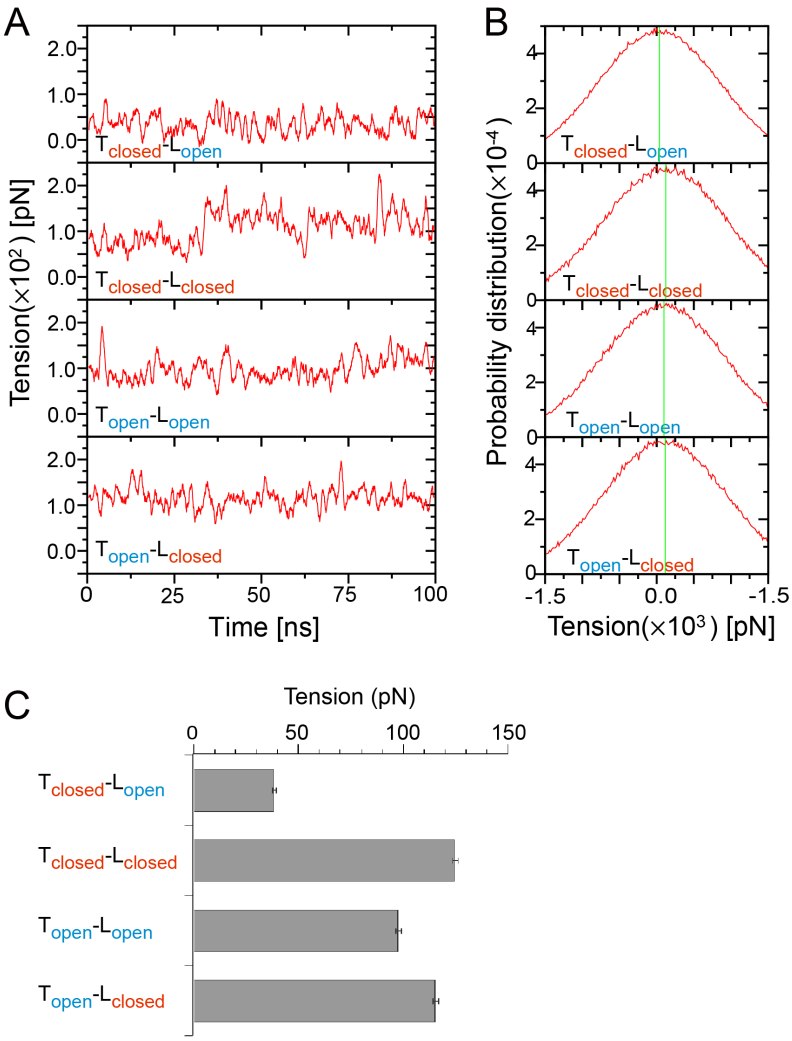

Figure 7. **Estimation of tension in the disordered neck linker region using MD simulations of refined dimer models. (A)** Time trajectories of the trends of tension during 100-ns simulations, using model systems (Fig. S4 D) derived from refined dimer models with various open and closed head combinations (Fig. 6). Tensions were calculated by multiplying the deviation of the Cα atoms at both ends of the disordered neck linkers from the potential minimum. The trend at each time *t* was calculated by averaging raw tension values within the time range [*t*-0.5: *t*+0.5] ns. Trends converged at ~35 ns for the T_{closed}-L_{closed} model and within 2 ns for the other three models. **(B)** Distributions of tension in disordered neck linkers, obtained from MD simulations. Green vertical lines indicate time-averaged tension for each state after convergence. **(C)** Time-average tensions and statistical errors for each state: 38.7 ± 0.8 pN for T_{closed}-L_{open}, 124.9 ± 1.5 pN for T_{closed}-L_{closed}, 98.1 ± 1.2 pN for T_{open}-L_{open}, 115.7 ± 1.2 pN for T_{open}-L_{closed}.

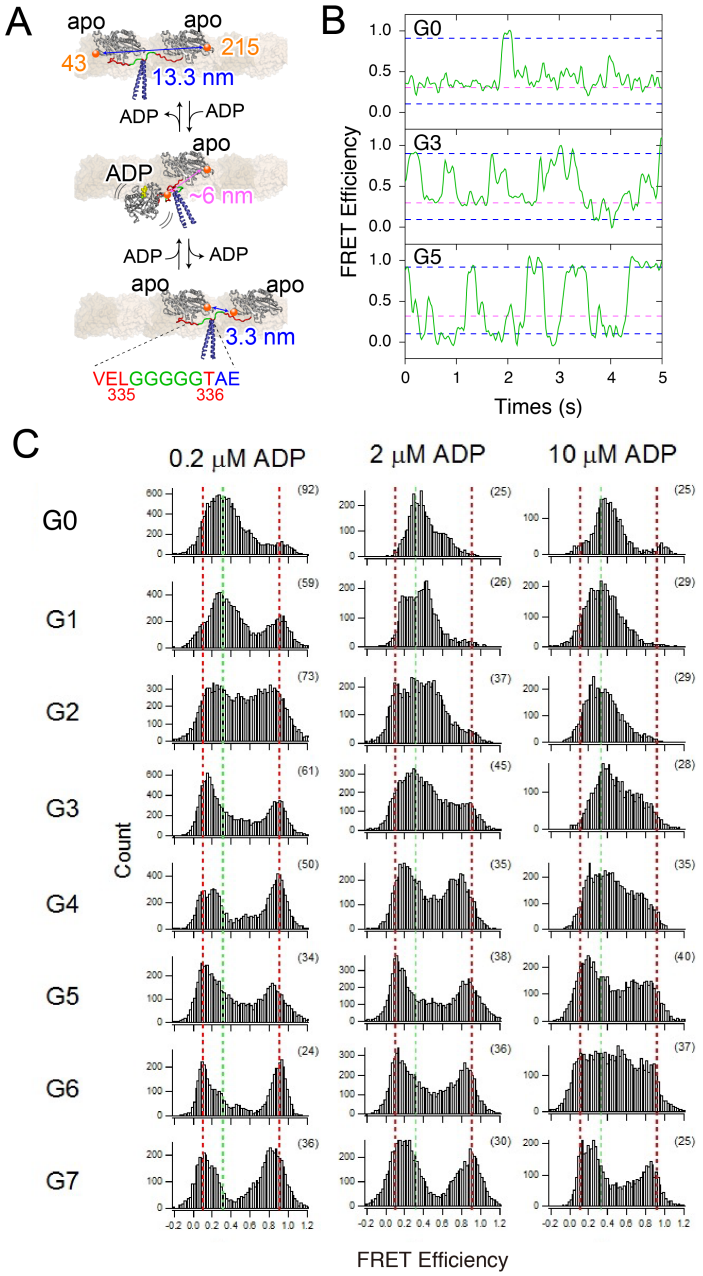

Figure 8. **Single-molecule FRET observations of conformational transitions of kinesin dimer with reduced neck linker tension.** (**A**) Schematic depicting off-pathway transitions from the two-head-bound state to one-head-bound states of a neck-linker extended mutant (5 poly-Gly insertion; green) without ATP. Positions of cysteine residues for labeling with FRET probe (215Cys on one head and 43Cys on the other head) are shown in orange spheres. (**B**) Typical FRET efficiency traces of Cy3/Cy5-labeled wild-type (G0) and neck linker extended mutants (3- and 5-Gly insertions; G3 and G5) bound to axonemes in the presence of 2 μM ADP. Blue and red dotted lines show previously reported peak FRET efficiencies for two-head-bound and one-head-bound states respectively (Mori et al., 2007). (**C**) Histograms of FRET efficiencies (from each frame of images) of Cy3/Cy5-labeled kinesin with varied neck linker lengths bound to axonemes in the presence of 0.2, 2 or 10 μM ADP. Occasional ADP binding to kinesin in the two-head-bound state reverts to one-head-bound state, and this frequency increases with higher ADP concentrations. Parentheses show the numbers of molecules analyzed. Dotted lines highlight peaks characteristic of putative two-head-bound (blue) and one-head-bound (red) states.

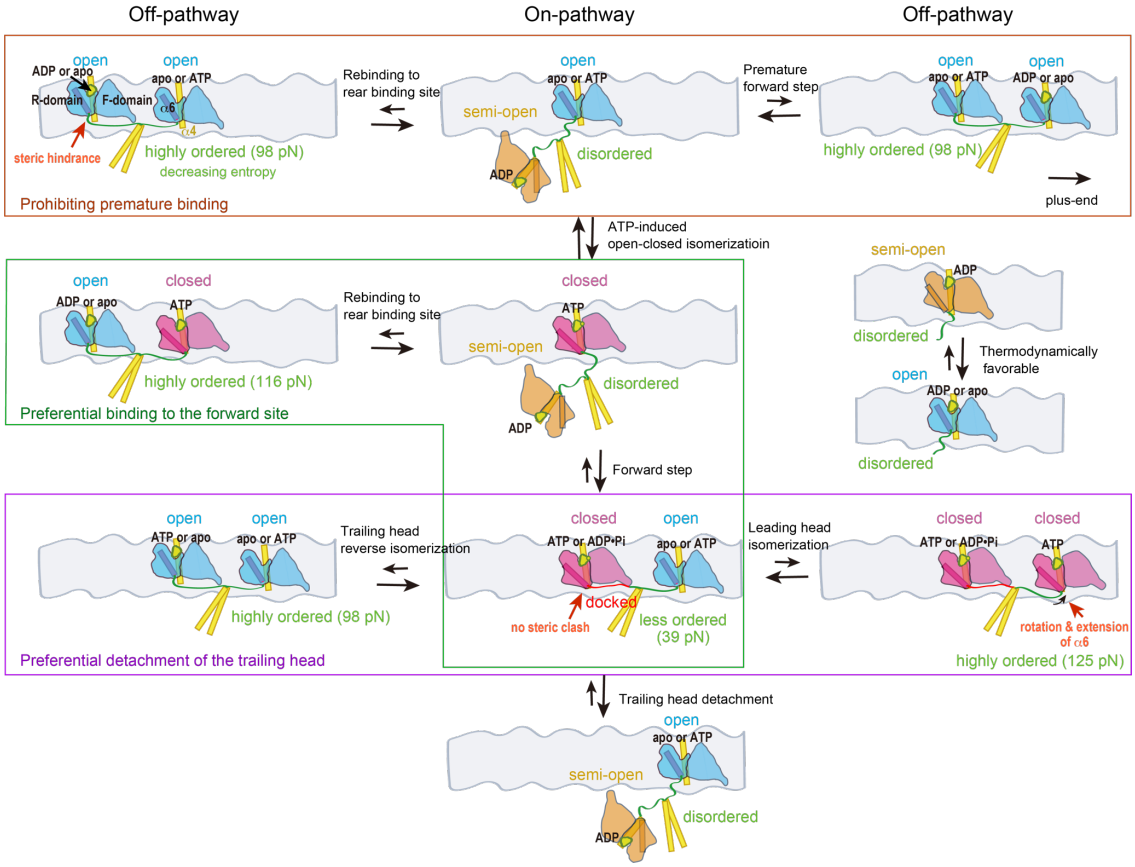

Figure 9. **Tension-based regulation mechanism explaining the coordinated stepping of kinesin-1 along the microtubule.** This model proposes that thermodynamically favorable transitions between a head's conformational states (semi-open to open, and open to closed) are regulated by entropy loss due to neck linker stretching in dimeric kinesin. The semi-open, open and closed conformational states of the head are indicated in orange, blue and red, respectively, with the α6 helix, which connects to the neck linker, highlighted as a rod. The neck linker is shown in green, while the α4 helix, which directly interacts with the microtubule, and the neck coiled-coil are yellow. Premature binding of the tethered semi-open head to the microtubule in the ATP-waiting state is prevented by an intolerable increase in neck linker tension, as it causes substantial entropy reduction (red rectangle). This contrasts with a monomeric head with a disordered neck linker, where the semi-open-to-open transition is thermodynamically favorable (right). Even after ATP-induced isomerization of the microtubule-bound head, increasing tension prohibits rebinding of the tethered head to the rear-binding site (green hexagonal box), enabling preferential binding to the forward site. In the two-head-bound state, the trailing and leading heads stabilize in closed and open conformations, respectively, explaining why the trailing head hydrolyzes ATP and detaches from the microtubule before the leading head (purple rectangle).

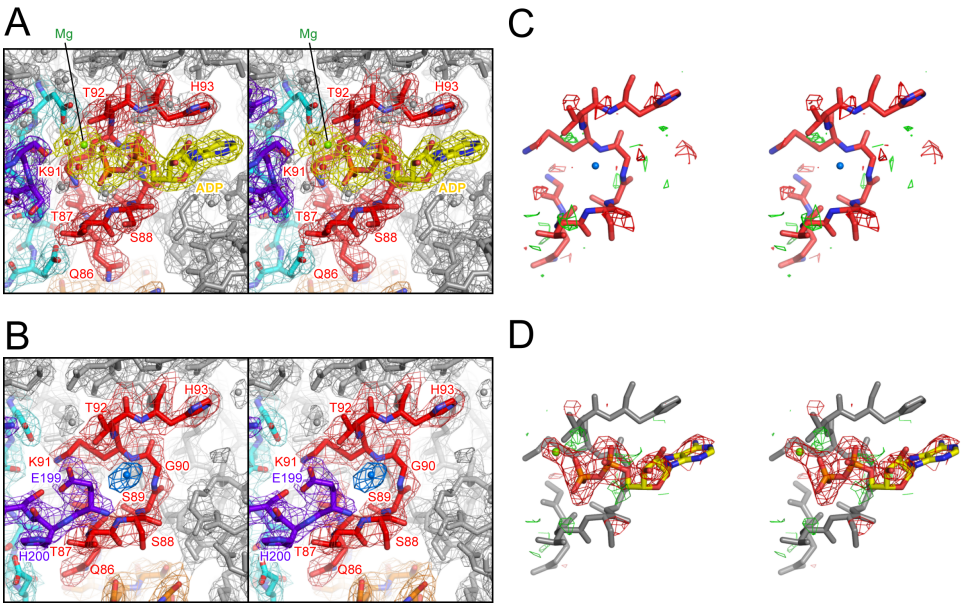

Figure S1. **Related to Fig. 1B. (A, B)** Stereo-views of the $2F_o$-F_c maps (σ = 1.0) around the nucleotide-binding P-loop (**A**: G234A kinesin complexed with ADP, **B**: G234A kinesin crystallized under nucleotide-free condition). ADP and Mg^{2+} ion are shown in yellow and lime green, respectively. **(C)** F_o-F_c difference map of the nucleotide-binding P-loop of nucleotide-free G234A mutant. Positive (σ = 2.0) and negative (σ = -2.0) densities are shown in green and red, respectively. No residual density was observed around the putative water molecule (blue). **(D)** F_o-F_c map (σ = ±2.0) obtained by one round of refinement after replacing the putative water molecule with MgADP in the nucleotide-free G234A model. The negative density (red) further clarifies the absence of MgADP in the nucleotide-binding pocket.

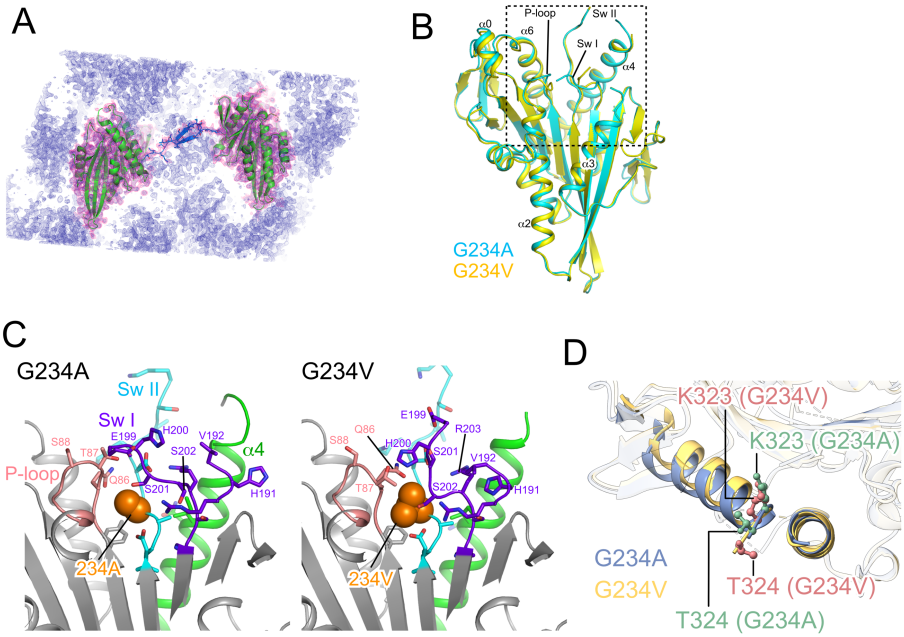

Figure S2. **2.8 Å crystal structure of nucleotide-free G234V mutant kinesin. (A)** The crystal packing of nucleotide-free G234V mutant. $2F_o$-F_c map is shown in mesh (dark-blue) and the densities around the asymmetric unit are colored in pink. The proximal ends of the neck linkers of chains A and B face each other, with a cylindrical cavity between them. This cavity allows an antiparallel β-sheet formation between the two stretched neck linkers of chain A and B (shown in blue). While this demonstrates the neck linker peptides have an ability to form antiparallel β-sheets, such an arrangement would be geometrically impossible for the two neck linkers in a dimer, as their C-termini are joined in parallel by the neck coiled-coil. In the G234A apo structure, we did not observe density corresponding to the antiparallel β-sheet in the cavity, likely due to its slightly smaller cavity size. **(B)** Comparison of the overall structures of nucleotide-free G234A (cyan) and G234V (yellow) crystal structures. G234V kinesin structure is nearly identical to that of G234A, except for the difference in the P-loop. **(C)** Close-up view of the nucleotide-binding pocket of G234A and G234V mutants (dotted rectangle in panel B). The side chains of residue 234 are shown as space-filling. The P-loop (pink) of G234V displayed a closed conformation, distinct from previously solved kinesin structures, indicating that the P-loop can adopt different configurations without bound phosphate. **(D)** Close-up view of the α4/α6 helices of nucleotide-free G234A (blue) and G234V (yellow) (the G234 structure is included from Fig. 1 C). The first two residues of the neck linker, K323 and T324, are highlighted as ball-and-stick models (G234A in green, G234V in red). In the G234V mutant, the T324 residue of the neck linker was visible and shifted toward the minus-end of microtubule compared to that of G234A.

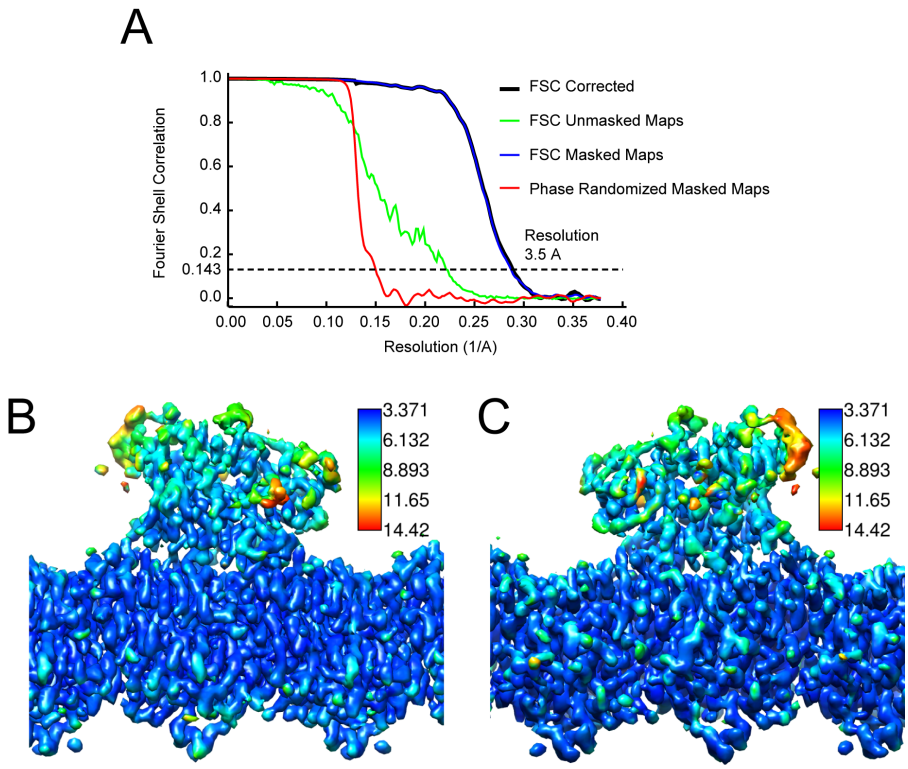

Figure S3. **Related to Fig. 2**. **(A)** Fourier shell correlation (FSC) curve for global resolution estimation, using a FSC 0.143 criterion. **(B and C)** Local resolution estimation from MonoRes (Vilas et al., 2018) with colors according to the color scale of left-side view (B) and right-side view (C). This local resolution map was used in local map sharpening (LocalDeblur (Ramírez-Aportela et al., 2020)).

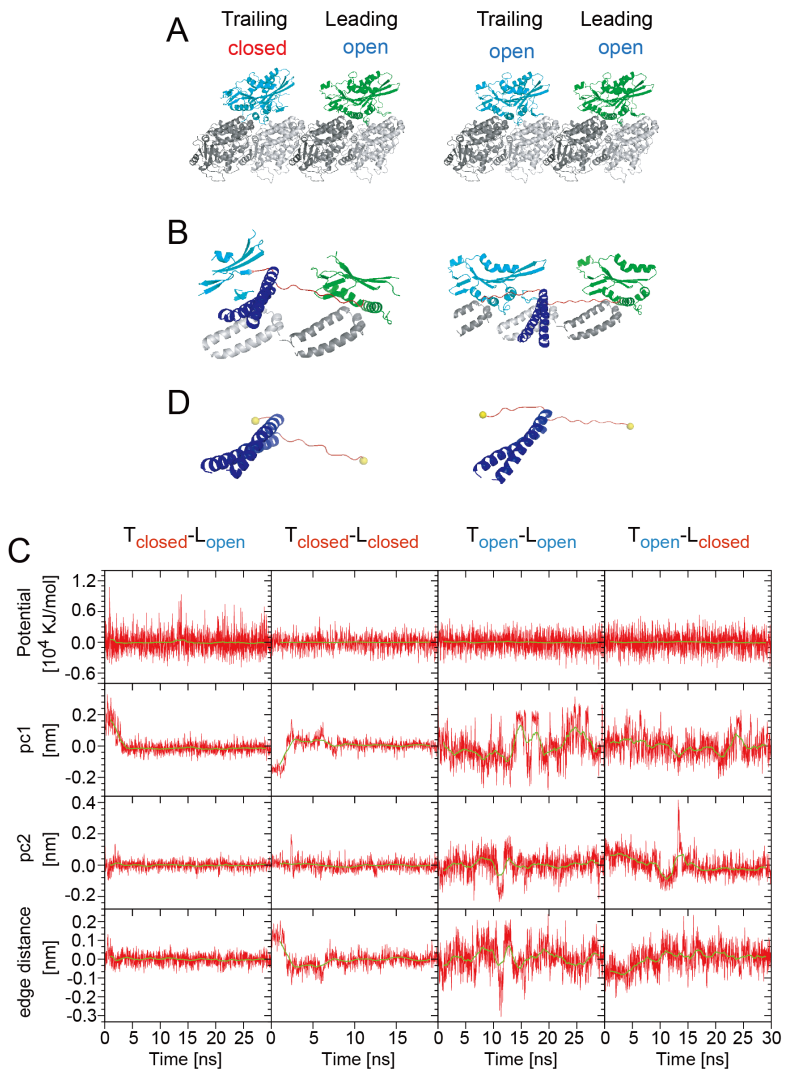

Figure S4. **Related to Fig. 7. (A)** Kinesin-microtubule complex models were initially created by fitting crystal structures to cryo-EM density maps (left: T_{closed}-L_{open}, right: T_{open}-L_{open}). Disordered regions—those invisible in the crystal structures—were excluded from this model. **(B)** The model systems used to estimate the thermally equilibrated conformation of the disordered neck linker region. Molecular dynamic (MD) simulations moved the disordered neck linkers (shown in red), while kinesin and tubulin residues within 12 Å from the neck linker (cyan, green) were position-constrained to act as steric hindrance. **(C)** Time trajectories of total potential energy, principal components (pc1 and pc2) from standard PCA, and end-to-end distances of the disordered neck linker, during MD calculation of four kinesin dimer models. End-to-end distances converged after 2-15 ns, indicating that the disordered neck linkers reached near-thermal equilibrium by the end of the simulations. Representative snapshots of equilibrium states shown in Fig. 6 were selected from structures after extended simulation periods. These structures had end-to-end distance and pc1/pc2 values nearly identical to the average values (< 0.01 nm deviation): t = 29.870 ns for T_{closed}-L_{open}, 19.920 ns for T_{closed}-L_{closed}, 12.758 ns for T_{open}-L_{open}, and 29.696 ns for T_{open}-L_{closed}. **(D)** Model systems used to estimate the tension on disordered neck linkers (Fig. 7). MD simulations were performed using the refined neck linker and neck coiled-coil (Fig. 6). Harmonic potentials were applied to the Cα atoms at both ends of the disordered neck linkers (yellow spheres; E334 for T_{closed} (left) and T328 for T_{open} (right), and I325 for L_{open}). Tension was calculated by multiplying the deviation of the Cα atoms from the potential minimum by the spring constant. Time trajectories are shown in Fig. 7 A.

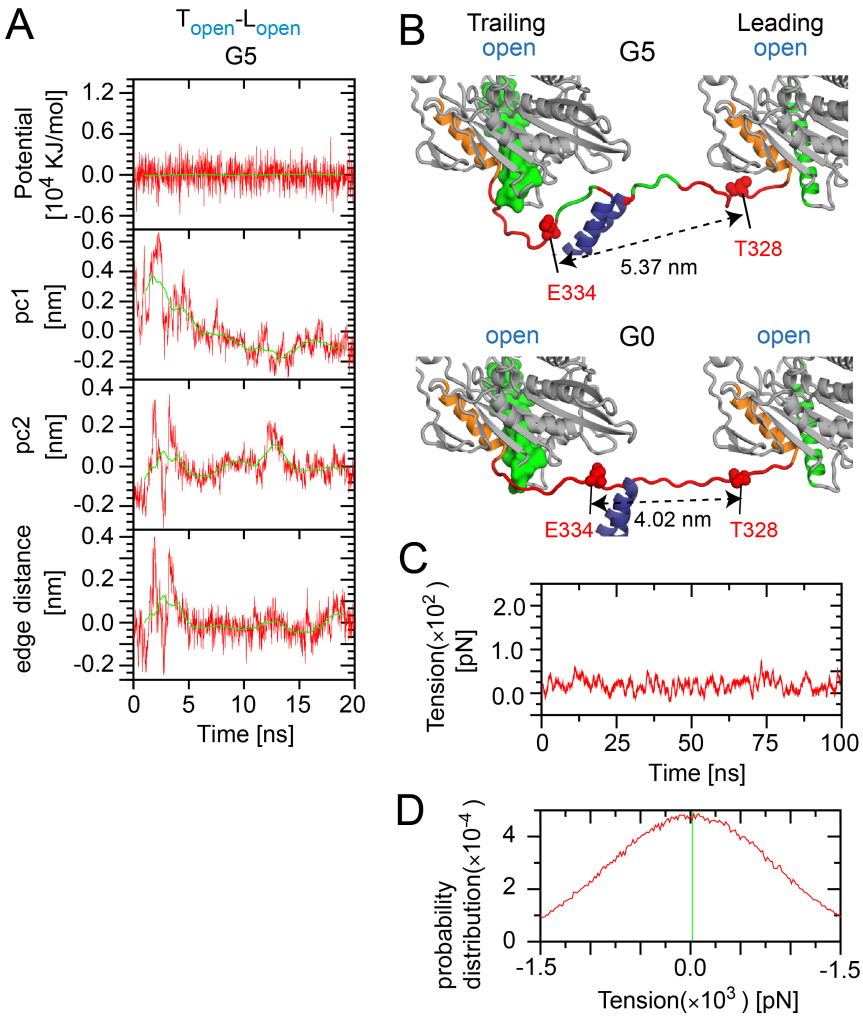

Figure S5. **Refinement structure of disordered neck linkers and its estimated tension of neck linker-extended mutant in T_{open}-L_{open} state.** (**A**) Time trajectories of total potential energy, pc1 and pc2 from standard PCA, and end-to-end distance of the disordered neck linker during MD calculation of G5 mutant in T_{open}-L_{open} model. (**B**) T_{open}-L_{open} model of G5 mutant compared with the T_{open}-L_{open} model without neck linker extension (G0). Thermally equilibrated conformation of the disordered neck linker was determined by MD simulation. Disordered neck linkers were isolated from the refined model, and harmonic potentials were applied to Cα atoms of residues at both ends (T328 in trailing head and I325 in leading head) to estimate tension. (**C**) Time trajectory of tension trends during 100-ns simulations. Trend at each time *t* was calculated by averaging raw tension values within the time range [*t*-0.5: *t*+0.5] ns. (**D**) Distribution of tension in disordered neck linkers from MD simulation. Green vertical line indicates time-averaged tension after convergence. Average tension, calculated using the data after the convergence, was 19.0 ± 1.2 pN.

Video 1. **Subdomain motions associated with the allosteric conformational changes of kinesin on microtubule (back-view).** The morph movie between semi-open, open and closed states, with subdomains color-coded. Related to Fig. 4 B.

Video 2. **Subdomain motions associated with the allosteric conformational changes of kinesin on microtubule (side-view).** The morph movie between semi-open, open and closed states, with subdomains color-coded. Related to Fig. 4 D.

Video 3. **Thermal motion of the disordered neck linkers in T_{open}-L_{open} or T_{apo}-L_{apo} state.** The movie shows molecular dynamic simulation for 16 ns. The disordered neck linker regions are shown in stick representation. Related to Fig. 6 A (left).

Video 4. **Thermal motion of the disordered neck linkers in T_{closed}-L_{open} or T_{ATP}-L_{apo} state.** The movie shows molecular dynamic simulation for 30 ns. The disordered neck linker regions are shown in stick representation. Related to Fig. 6 A (right).